NUREG/CR-0914
SAND79-0940
R7

1361 115

VISUAL INVESTIGATION OF REACTOR FUELS RESPONSE TO SIMULATED LOF HEATING CONDITIONS, FIRST SERIES

G. L. Cano, R. W. Ostensen, M. F. Young

Printed October 1979

Sandia Laboratories

Prepared for

U. S. NUCLEAR REGULATORY COMMISSION

323

Available from
National Technical Information Service
Springfield, Virginia 22161

NUREG/CR-0914
SAND79-0940
R-7

VISUAL INVESTIGATION OF REACTOR FUELS RESPONSE TO SIMULATED LOF HEATING CONDITIONS, FIRST SERIES

Gilbert L. Cano
Raymond W. Ostensen
Michael F. Young

Date Published: October 1979

Sandia Laboratories
Albuquerque, New Mexico 87185
operated by
Sandia Corporation
for the
U. S. Department of Energy

Prepared for
Division of Reactor Safety Research
Office of Nuclear Regulatory Research
U. S. Nuclear Regulatory Commission
Washington, D.C. 20555
Under Interagency Agreement DOE 40-550-75
NRC FIN No. A1016

ABSTRACT

In a loss-of-flow (LOF) accident in an LMFBR, the mode and timescale of disruption of fuel can establish the probability of a subsequent energetic excursion. To investigate these phenomena, in-pile disruption of internal-fission-heated fuel pellets, both fresh UO_2 and preirradiated mixed oxide, was recorded by high speed cinematography. Neither fuel frothing nor dust-cloud breakup occurred under the simulated LOF conditions. Instead massive and very rapid fuel swelling, not predicted by current transient fuel-swelling and gas-release models, occurred. This may be the initial and dominant mode of fuel disruption in an LOF. A new transient fuel-swelling model, FISGAS, has been developed at Sandia.

CONTENTS

1361 119

TABLES

ILLUSTRATIONS

1361 121

1. Introduction

An area of considerable importance in reactor safety is the fuel behavior in a hypothetical unprotected loss of coolant flow (LOF) accident in LMFBR's. In fact, much of the experimental and theoretical research pertinent to hypothetical core disruptive accidents (HCDA) in fast reactors has been concentrated on LOF scenarios. The main instrument for calculating different aspects of core behavior in such a hypothetical LOF accident path has been the SAS computer code, described elsewhere.[1,2] In general, SAS models and calculates effects on reactor fuel, clad, and coolant of initially imposed reactivity ramps and coolant flow perturbations and the reactivity feedbacks of these effects. However, as for other possible accident paths, insufficient experimentally determined data has been available to aid in development of SAS, and for verification of its analytic and predictive capabilities for an LOF sequence.

An LOF accident can occur in an LMFBR core in several ways. Power failure to the coolant pumps, for instance, can produce LOF conditions. The pumps coast down and coolant flow decreases leading to sodium boiling and voiding in the core. In the proposed Clinch River Breeder Reactor, CRBR, the result would be insertion of positive reactivity and a consequent power rise. In any case, the early-time fuel response to the ensuing power rise is of prime importance.

In an LOF, occluded fission products, primarily gases, in the fuel have the potential to produce rapid fuel disruption such as swelling or rapid dispersal during the heating phase. If fuel pin disruption occurs, dependent on the mode and timescale of disruption, redistribution of fuel can have a dominant effect on the probability of a subsequent energetic excursion. The net effect of fuel dispersal can be significant negative reactivity and non-energetic accident termination. In the case of disruption through swelling, melting or slumping, however, a recriticality can occur. Thus the question of initial fuel behavior and the timescale for disruption or dispersal, if either of these occurs, must be addressed. This need is emphasized in the existing large discrepancies between the SAS-3A analyses of postulated LOF accidents performed by the DOE CRBR Project and those performed by the NRC staff.

The results of a SAS-3A best-estimate analysis of the CRBR LOF accident by McElroy, et al.[3] for the project office is shown in Figure 1. Shown are the reactor power and reactivity from the start of pump coastdown through accident termination under the main assumption of fuel dispersal. The fuel and coolant heat up at near-constant power for about 12.5 s until coolant boiling begins in the highest power channels. Boiling progresses to channel voiding and increase in reactivity and power. Thermal-reactivity feedback effects produce oscillations in the power history, and keep the reactor from achieving prompt criticality until pin failure occurs around 15.6 s. At this time fission-gas-driven fuel dispersal is invoked leading to a large decrease in reactivity and power and a safe reactor shutdown. According to this calculation, the peak power level reached during disassembly is about 90 times nominal and occurs about 2 s after sodium voiding.

In contrast, the results of a similar calculation using SAS-3A for the same LOF accident, but now done by the NRC[4] are shown in Figure 2. A number of differences occurred in the calculations, such as slight geometry and design modifications

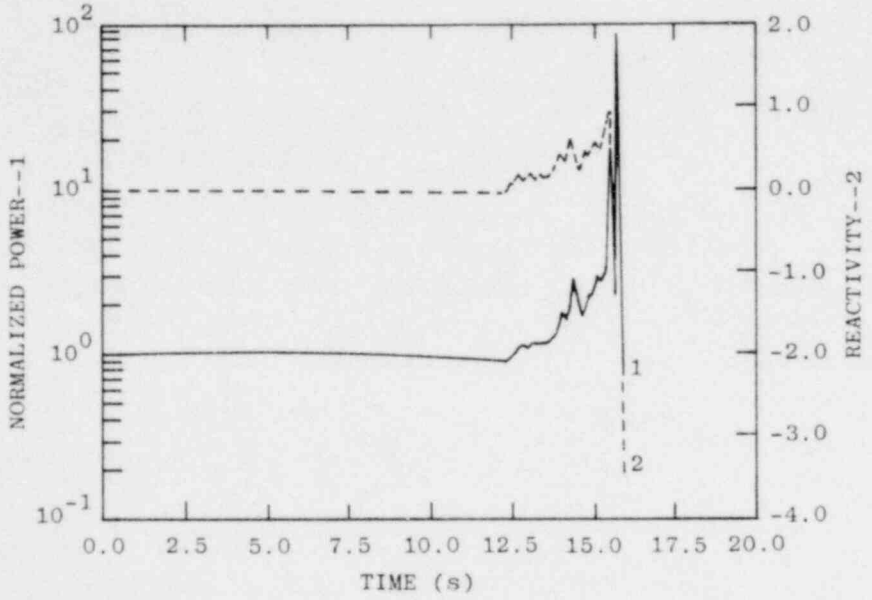

Figure 1. Power and Reactivity vs. Time.

1361 123

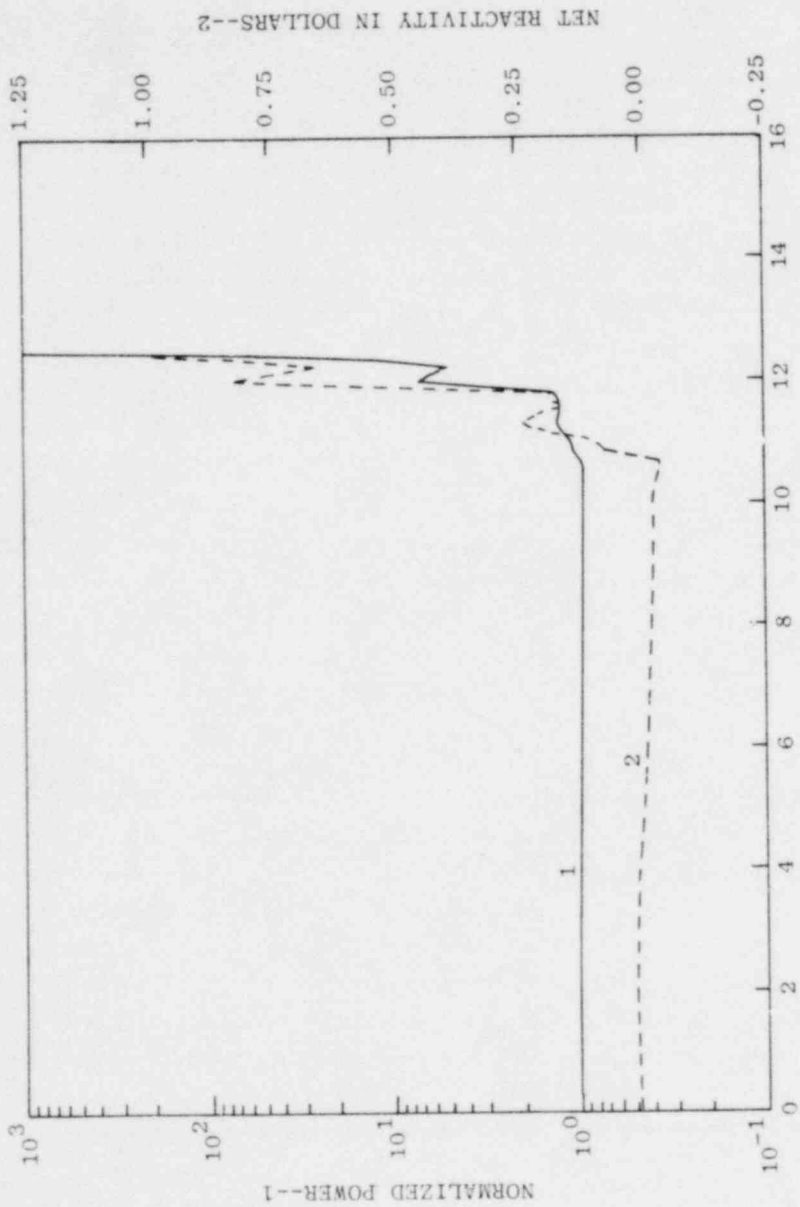

Figure 2. Power and Reactivity vs. Time.

1361 124

and coolant flow rate in some of the channels. The major difference between this and the project calculations, however, is that Meyer, et al.[4] explicitly prohibit fission-gas-driven fuel dispersal. In this case only fuel melting and slumping occur and the core power increases leading to significant work potential and possibly to vessel breach in an energetic accident termination. Thus, from these two contrasting examples it is evident that the question of initial fuel disruption in an LOF accident in fast reactors is crucial; the potential consequences of such a hypothetical accident establish the motivation for fuel disruption research, particularly in the experiment arena.

Understanding of fuel behavior in an LOF sequence has been based primarily on a number of experiments[5,6] which, with some exceptions, have been conducted ex-reactor by means of indirect or direct electrical heating of the fuel. Such experiments have provided valuable information on temperature behavior of gas release and swelling in slow transients. However, with the exception of the gas release data, the results have been obtained principally through inferences from post-test examinations of the remaining fuel. Some fuel disruption information has been obtained during tests by means of the neutron hodoscope and gamma-ray video monitoring. However, the fuel motion information so far obtained remains inconsistent, and hard data on initial fuel disruption modes and timescales have been absent.

There has been some evidence of fission-gas-driven fuel disruption and dispersal with foaming or frothing of molten fuel, dust-cloud disassembly in the solid state, or fuel swelling[5]. However, swelling is not detected unequivocally by the neutron hodoscope, and in the experiments the observed post-test swelling could have occurred after the active phase of the experiment. In addition, fuel swelling rates have not been obtained previously. In fact, one current assumption[2] is that swelling occurs only under low heating rates ($\lesssim$200 K/sec) and that it probably is not a factor at high power levels of interest in LOF sequences, or in mild to high power burst conditions. Similar types of notable uncertainties occur with the other data observed, most of which have been for non-prototypic fuel-heating conditions and some of which have not proven to be reproducible in numerous attempts. Using this limited data base, models for analysis and prediction of fuel behavior have been developed. Thus, with the goal to strengthen and extend the data base for correct model development, a program of in-reactor experiments which address principally the questions of mode and timescales of disruption, or dispersal of preirradiated oxide fuel pins was undertaken at Sandia Laboratories. A more in-depth introduction to this subject may be found in References 5 and 6.

2. Sandia Fuel Disruption Experiments

Several designated series of experiments are being conducted in the fuel disruption area in which both preirradiated fuels and fresh fuels are subjected individually to similar power transients illustrative of LOF sequences. It is anticipated that the experiments will investigate not only oxide (UO_2) and mixed oxide (U/PuO_2) fuels, but also more advanced fuels such as carbides, metal, and thorium fuels and other accident paths, as necessary. Concurrently, a comprehensive experiment analysis and model validation and development effort is being carried out. The end product of this coupled research should be proven fuel behavior models for use in hypothetical core disruptive accident code predictions and analyses. Generally, the two factors controlling fuel disruption in an LOF sequence are believed to be the rate and amount of fuel heating, and the amount of volatile fission products, primarily gases, accumulated in the fuel.[5,6] The fission product content of a given enrichment fuel is determined by its steady state linear power output and its heavy-atom percent burnup. Thus, investigation of the response of LMFBR fuels to LOF accident conditions should revolve around these parameters. Tests on a given type of fuel may begin with small sections, such as a single pellet and proceed to full fuel elements from pins of equal burnup percent but with different heat ratings. Alternatively, the linear heat rating can be fixed and the fissile-atom percent burnup can be varied. Both options should be examined for a variety of LOF heating sequences which, according to calculations, could occur in LMFBR's. The tests should investigate the range of linear heat ratings and the region of burnup from zero, or very low, to the maximum design goal of 10% for breeder reactors.

Because initial fuel disruption is of primary interest, it is necessary only to achieve the proper temperature profile and history in the fuel as have been calculated for various LOF sequences.[7] It is not necessary to perform the experiments in a prototypic environment such as in a subassembly with flowing sodium or sodium vapor.

Consideration was given to the length of the fuel element necessary to simulate breakup behavior of a full pin. The fuel disruption is basically a one-dimensional phenomenon; there is little or no axial effect within a fuel pin. For short fuel segments, the axial load should simulate the effect of the weight of half the fuel column as well as the load due to any axial swelling. The axial constraint applied may be considered prototypic if it does not lead to any significant crushing of the fuel, and does not allow substantial axial swelling. This was the case for most of the tests of interest in this program.

At experiment time the conditions of the test fuel must be realistic, both physically and chemically. This means the fuel must not be mechanically disturbed prior to the test, such as would occur upon removal of the fuel from its clad, and that if a pin is cut to extract a particular section for an experiment, the cutting, handling and loading must be controlled to avoid contaminants. Even slight disassembly of the fuel can allow escape of fission gases, and it also can weaken intergranular binding such that a particular type of disruption may be favored, or prevented. With reference to contaminants, it has been found[8,9] that fuel

cut in a nitrogen atmosphere containing 300 ppm impurities contains significantly more N_2, H_2, and CO than can be expected from "known" contamination in fuel and pin fabrication. Thus, although intensive investigation still is needed in this area and the source and effects of contaminants have not been determined, exclusion of additional contaminants is requisite.

3. Initial Series of Fuel Disruption Experiments, FD-1

3.1 Purpose and Experimental Approach

The broad purpose of the first series of tests was to study, by means of cinematography, the phenomenology of fuel behavior, in pile, for such LOF accident conditions as could be simulated in the Sandia Annular Core Pulsed Reactor, ACPR. If successful, this would provide the first visual determination of the actual modes and timescales of reactor-fuel failure. A variety of power and energy levels internally-fission-generated in the test fuel, and a variety of fuel parameter values were to be used. Also, the large-scale effects of occluded fission gases and other products on fuel disruption could be studied by comparing irradiated fuel behavior with fresh fuel behavior under otherwise similar conditions. Then, using the data obtained from the experiments, existing fuel behavior models and codes were to be tested for accuracy and applicability. Modification of these models and codes could be guided by the results. Also, new models and codes could be developed and verified, thus leading to better understanding of fuel disruption phenomena.

The experimental approach was to expose a single pellet of preirradiated mixed oxide fuel or fresh UO_2 fuel, to multiple neutron-pulses in the ACPR, and simultaneously to record in real time the fuel response to the transient power conditions by means of high speed cinematography. It was requisite that the fuel, if preirradiated, be in its original cladding and mechanically undisturbed. The neutron multipulsing was necessitated by limitations in programmed high power operation in the ACPR, and the need to achieve sufficient heating and suitable temperature profiles which would be at least near the "calculated prototypic" conditions of the hypothetical LOF. In fact, in order to achieve the necessary energy generation in the fuel, a neutron moderator (polyethylene) had to be placed between reactor and experiment vessel.

The most novel aspect of the experiments was the use of high speed cinematography from outside of the reactor, to record the fuel response to the transient in-pile fission-heating for subsequent detailed analysis.

A series of eleven experiments was designed because the fuel used in a given test would be disrupted in a single multipulse exposure and it was necessary for a pragmatic investigation to begin with little disruption on the first pellet and to proceed through complete fuel dispersal on others. Nine of these were to use preirradiated fuel and two were to use fresh UO_2 fuel. In actuality twelve tests were conducted, as described later.

Finally, the potential fuel disruption modes expected in these experiments included disruption of the fuel in the solid state as a dustcloud; or disruption as a liquid foam or froth; or by fuel melting and slumping; or by gross swelling of the fuel.

3.2 Experiment Method and Execution

According to Bohl[10], the radial temperature distribution at disruption in an LMFBR fuel pin is peaked at the centerline at 3020 K, the melt temperature, and decreases to about 2400 K at the fuel surface. The axial temperature variation is small and negligible. Thus, it was desired to achieve temperature profiles

at pellet disruption which at least approximated these predictions. Attainment of such a profile in the fuel available by means of the ACPR required use of the multiple pulse technique. This was established by means of neutronic and heat transfer calculations which are discussed in Section 3.3.

The fissile-atom enrichment of the fuel and the energy spectrum of the moderated neutrons incident upon it in a single pulse were such that the calculated axial and radial energy generation profiles in the fuel were cupped with a peak-to-minimum (P/M) ratio as large as 4. This P/M ratio could be reduced by use of thinner or no moderator. However, moderator was required in order to produce enough energy in the fuel to reach the temperatures sought. Each pellet, in its clad, was to be subjected in a single ACPR test to a double or triple pulse with each individual pulse a few tens of milliseconds full width at half maximum intensity. In a given test, multiple pulses with enough time between individual pulses for temperature profile inversion were to be utilized. For a given multipulse energy, the internal energy state of the fuel could be varied by varying the time between individual pulses from one test to the next. In a given enrichment fuel, higher temperatures were to be achieved in tests with shorter intervals between pulses due to reduced heat loss prior to the final pulse.

According to calculations, the irradiation was to produce fuel heating to the melting point ±550 K, depending on the test. This variation was to be accomplished by keeping the energy produced in the ACPR the same for a given pulse mode, and varying the time between individual pulses from 1 s to ½ s.

The FD-1 series consisted of 12 experiments. Ten of these utilized a total of nine preirradiated mixed oxide fuel pellets, one per test, and the other two experiments used fresh UO_2. One preirradiated pellet was used in two tests which served for calibration and diagnostics.

Figure 3 illustrates the experimental arrangement. The back-lit fuel sat on a depleted urania button which served as a thermal insulator and which was embedded in a graphite block. The pellet was held in place by a similar urania-graphite cylinder attached to a spring loaded clip which simulated the axial pressure loading on the fuel as exists in reality in the fuel pins. The fuel center coincided with the center of the reactor core.

Photography involved relaying an image of the pellet about 10 meters via a number of mirrors along the line-of-sight pipe of the reactor to and through an offset loading tube to a Questar telescope. The Questar's output formed the object for a Fastax recording camera.[11] The pellet response to the power transient was recorded on Eastman Kodak RAR 2479 film which has a dynamic range of 1000:1. The frame rate was 450 to 2800 per second for a few seconds, depending on the test.

Photometric radiometry was employed to determine temperatures. This method utilizes a point-by-point comparison of the emulsion density on the film exposed to the hot fuel's optical radiation to the density produced on the same film by a National Bureau of Standards calibrated light source and the same optical path. The temperature range selected for investigation included 2200 K to 5000 K. Thus the temperature of the clad, which melts at 1670 K, could not be evaluated, with the exception of time of melt as seen on the film. The radiometry method and formulation are given in the literature.[12]

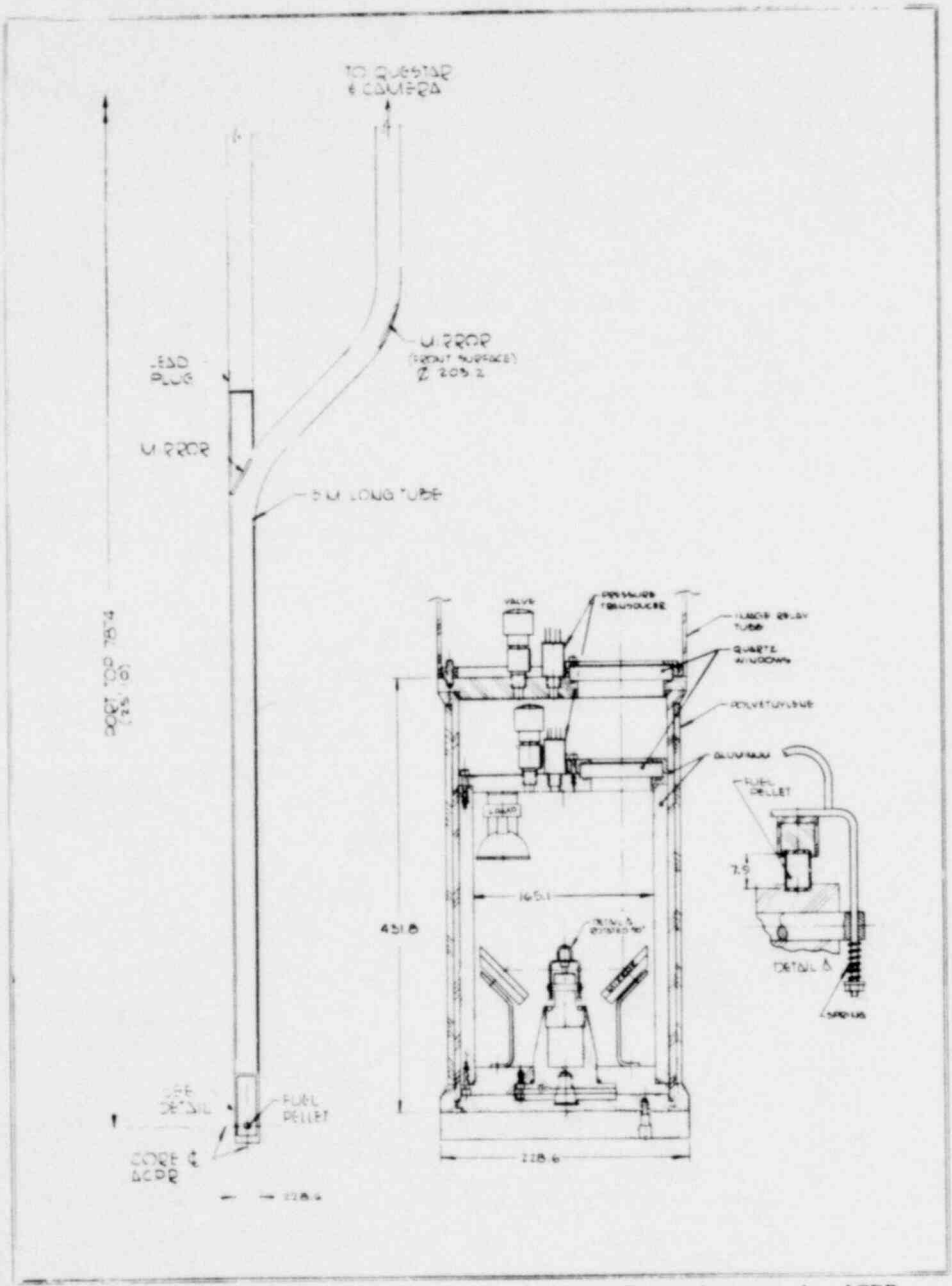

Figure 3. Capsule for Fuel Disruption Experiments in ACPR. All Dimensions are in Millimeters.

1361 130

The mixed oxide fuel pins were irradiated in EBR-II. For these experiments, three pins were sectioned in a nitrogen atmosphere, at LASL, to obtain from each pin three single, intact pellets in their clad. For each pin, one pellet was taken from a location near an end, another from a location near the center, and the third pellet from a location about midway between the other two. Sectioning included the extraction of a thin wafer(≈1 mm) of the pellet adjacent to each end of the pellet selected for each experiment. The purpose of including the wafers in the sectioning was to assure that the test pellets were not mechanically disturbed or damaged during the sectioning operation.

Figure 4 shows the origin of the pellets selected from each pin and the number of the experiment in which each pellet was used. Also, shown are views of one end, as cut, of the pellet taken from the midsection of each pin. The heavy-atom percent-burnup of the three pins is approximately 5%; the linear power output of each differed while in EBR-II, as shown. An effect of this is seen in the growth and size of the central void. The two pellets of fresh fuel, prepared at LASL, had fissile atom enrichment of 70% and were comparable to one of the mixed oxide fuels used. Table 1 contains data pertinent to these fuels.

Finally, not only could photographic records be obtained for detailed analysis of the real-time fuel response to the power transient, but also the fuel would be available for detailed posttest microanalysis of melt fronts, voids and cracks generation, for fission-gas-bubble morphology, for clad analysis, for isotopic analysis, and for investigation of swelling processes and locations, as necessary.

3.3 Pretest Neutronic and Heat Transfer Analysis

3.3.1 Introduction

Two-dimensional neutronics calculations using TWOTRAN[13] were performed[14] using the bare-cavity neutron fluence as given in the ACPR Experimenter's manual,[15] for a range of polyethylene moderator thicknesses, and the fuel to be used. These calculations indicated that for any neutron pulse from the ACPR the pellets would have axial and radial P/M energy deposition ratios of 2-4 with the peak occurring on the fuel surface.

Thus it was necessary to find a technique which would allow for rapid heat transfer from the fuel to the clad and relaxation of the inverted temperature profile. This would achieve the experiment goals of having (1) either uniform fuel temperature or temperature decreasing from center to surface of the pellet at time of fuel melting, and (2) clad meltoff before fuel melting to allow for fuel behavior observation. It was determined that multiple pulse operation of the reactor in each experiment would partially accomplish these objectives. The time between pulses in a multipulse sequence could be varied to allow more or less heat transfer to occur, as necessary. The disadvantage of this operating mode was the reduced maximum reactor power output (70 MJ for a triple pulse versus 108 MJ for a single pulse) and consequent lower energy generation in the fuel pellet.

The TWOTRAN energy deposition results were used, in lieu of dosimetry data, together with a Fuchs-Hansen[16] model simulating the triple ACPR pulses, as input for a two-dimensional transient heat transfer calculation with TAC2D.[17] The

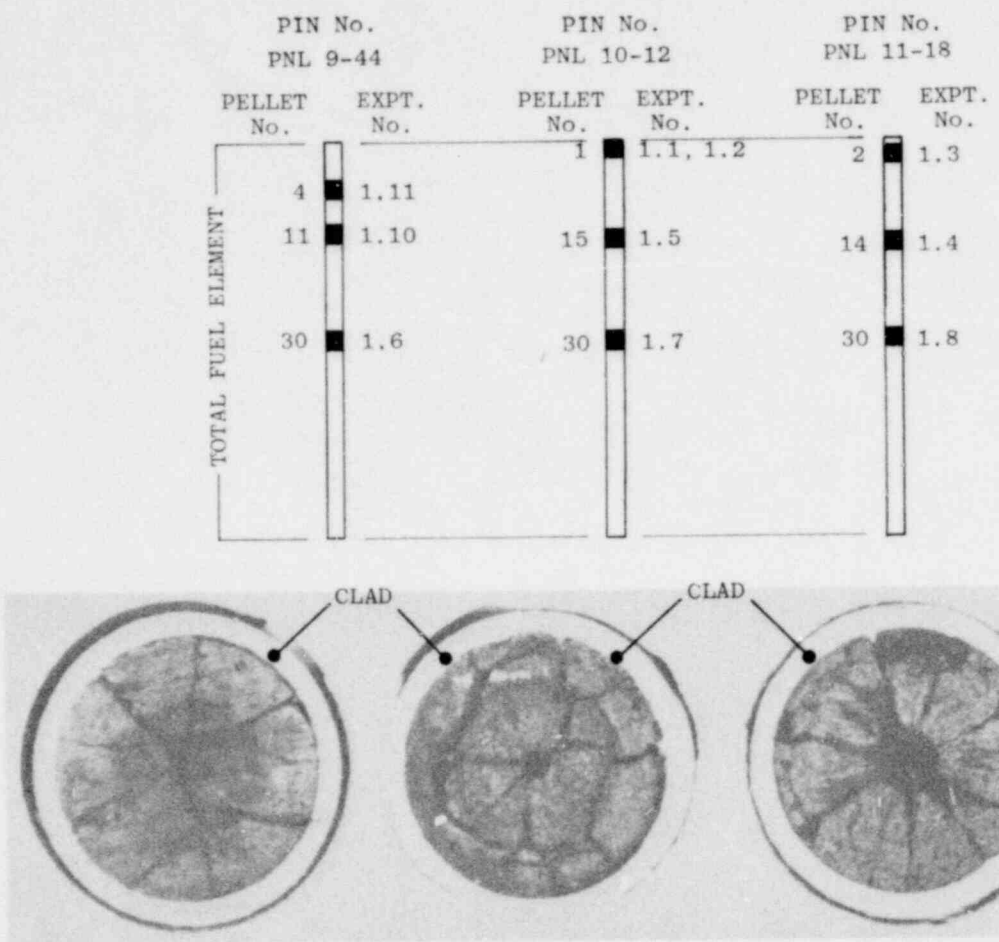

Figure 4. FD-1 Experiments Preirradiated Fuels Origin and Cross-Sectional Views, as Cut.

Table 1. FD-1 Experiments Fuels Data

Pin Number	PNL 9-44	PNL 10-12	PNL 11-18	Fresh UO_2
$\frac{PuO_2}{UO_2 + PuO_2}$	25%	25%	25%	0
$\frac{\text{Fissile Atoms}}{\text{Total U + Pu Atoms}} = e$				
@ Fabrication	44.5%	70.7%	70.8%	70%
@ Expt. Time	40.5	67.1	67.7	70
Linear Power, Pin Avg.	16.3 kW/m	26.3 kW/m	33.1 kW/m	--
Heavy Atom % Burnup, Peak	4.9	5.4	4.7	0
Fuel Sintered Density	9.88 g/cm^3, 90.1% TD	10.06 g/cm^3, 91.8% TD	9.96 g/cm^3, 90.9% TD	9.74 g/cm^3, 89% TD
Pellet Length, Ave.	0.546 cm	0.569 cm	0.572 cm	0.585 cm
Clad Material	20% CW 316 SS	20% CW 316 SS	20% CW 316 SS	20% CW 316 SS
Clad Outside Diameter, Avg.	0.588	0.591 cm	0.589 cm	0.585 cm

results indicated that for a triple pulse, 0.313 cm of moderator with the 40% effective enrichment PNL 9-44 pellets, and no moderator with the 68% effective enrichment PNL 10-12 and PNL 11-18 pellets would drive the pellets to the solidus.[18] Also, the clad would melt off between the second and third pulses.

3.3.2 Neutronics

Pretest neutronics were performed[14] with TWOTRAN,[13] a two-dimensional neutron transport code, using nine energy groups and the Sn_4 approximation. The ACPR core, experiment capsule and test pellet were modeled for a range of polyethylene moderator thicknesses from 0 to 9.525 mm and effective fuel pellet enrichments from 48% to 78%, the as-fabricated values. The pellet itself was represented by a 6.4 mm-high by 2.43 mm-radius cylinder divided into 4 radial nodes and 4 axial nodes. Both UO_2 and PuO_2 neutron cross-sections were included, although it was determined that the difference in energy deposition between UO_2 and UO_2/PuO_2 was negligible for cases of interest here.

The raw data for each enrichment/moderator thickness combination was fitted by averaging and least squares to an equation of the form

$$f(r,z) = N\left[1 + A(r/R)^2 + B(z/H)^2\right],$$

where

$f(r,z)$ = energy deposition shape

$A = (PMR - 1)$

$B = (PMZ - 1)$

$N = 1/(1 + \frac{A}{2} + \frac{B}{3})$ = normalization

R = pellet radius

$H = \frac{1}{2}$ pellet height

PMR = average radial P/M ratio

PMZ = average axial P/M ratio

Although this equation is not the best possible fit to the energy deposition shape, it allows easy interpolation to different enrichment/moderator combinations. The results for radial and axial P/M and average energy deposition per MJ reactor yield are presented in Table 2. Figures 5 and 6 are the curves used for interpolation.

3.3.3 Heat Transfer

Results of the neutronics analysis and reactor power traces from the ACPR Experimenter's Manual[15] were used as input for the two-dimensional transient heat transfer code, TAC2D.[17] Material properties from ANL-CEN-RSD-76-1[18] were used to model the UO_2/PuO_2 fuel (initially, UO_2 properties were used), SS 316 cladding, and depleted UO_2 end buttons. See Figures 3 and 7. Graphite and aluminum properties are from Ref 19 and 20. Helium properties were calculated from formulae in Ref. 21. The effective heat transfer coefficient from the clad surface to the cannister wall was calculated as 5.8×10^{-5} W/cm^{2}K. Radiation (5% effect) and convection were neglected. The heat transfer coefficient across the fuel-clad gap was calculated to be 3 W/cm^{2}K, assuming helium in the gap and an accommodation coefficient of 1 for rough fuel and clad.[22]

Table 2. Energy Deposition Parameters

Polythickness	0 cm			0.635 cm			0.9525 cm		
Effective Enrichment	P/M_R	P/M_Z	E*	P/M_R	P/M_Z	E*	P/M_R	P/M_Z	E*
40.5%(1)				2.68	2.28	(4.91)	2.42	2.41	(5.38)
47.5%	2.29	1.79	(3.88) 4.28	2.56	2.03	(5.52) 5.42	--	--	--
67.1%(2)	3.07	2.42	(5.05)	--	--	--	4.02	3.07	(7.26)
67.7%(3)	3.10	2.44	(5.09)	--	--	--	4.05	3.10	(7.31)
70.0%(4)	3.15	2.45	(5.19) 5.15	--	--	--	4.15	3.15	(7.41)
73.8%	2.76	2.08	(5.37) 5.11	--	--	--	--	--	--
77.5%	2.83	2.10	(5.56) 5.39	--	--	--	--	--	--

(1) PNL 9044 End of Life (EOL)

(2) PNL 10-12 EOL

(3) PNL 11-18 EOL

(4) 70% enriched UO_2

* cal/g/MJ

Energy deposition in () are from dosimetry curves; others are TWOTRAN.

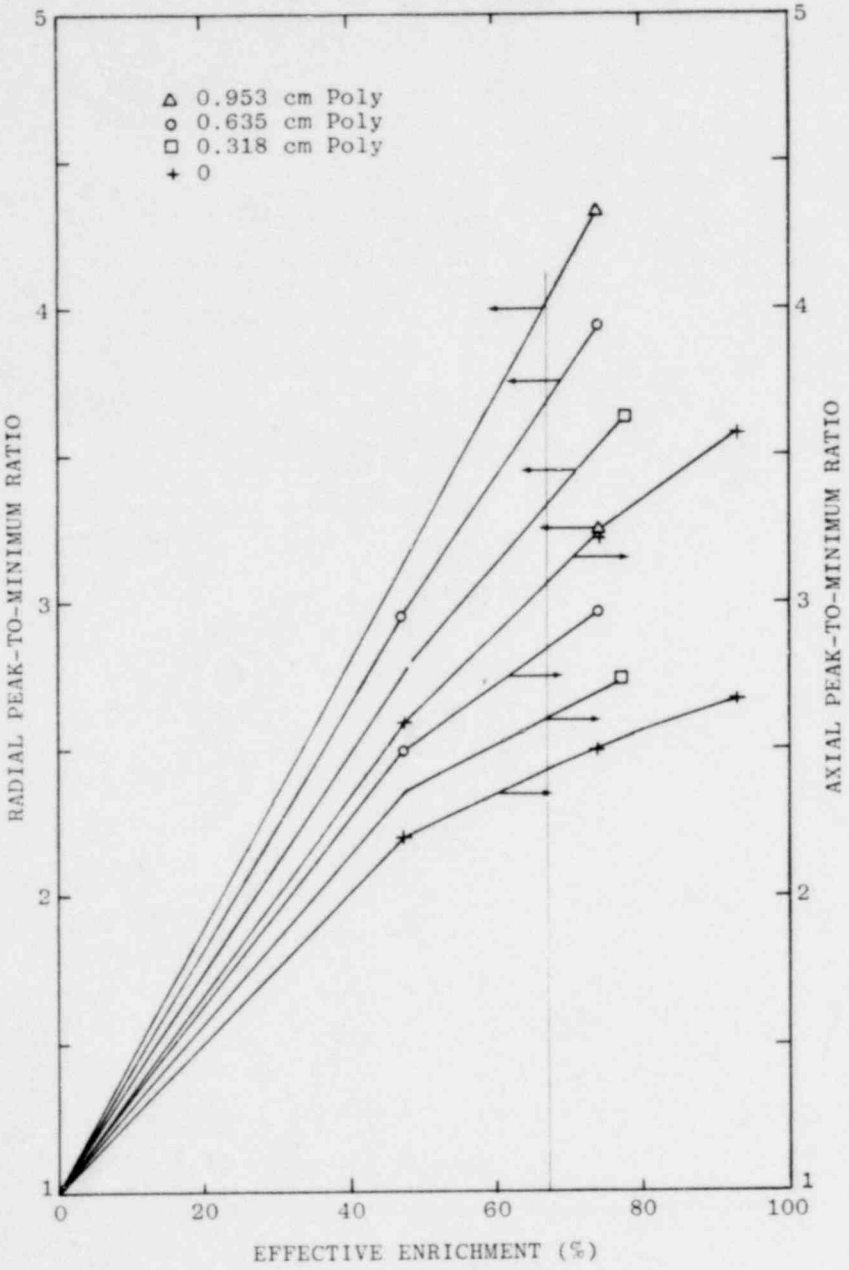

Figure 5. Peak-to-Minimum Ratios vs. Enrichment for Various Polyethylene Thicknesses.

1361 136

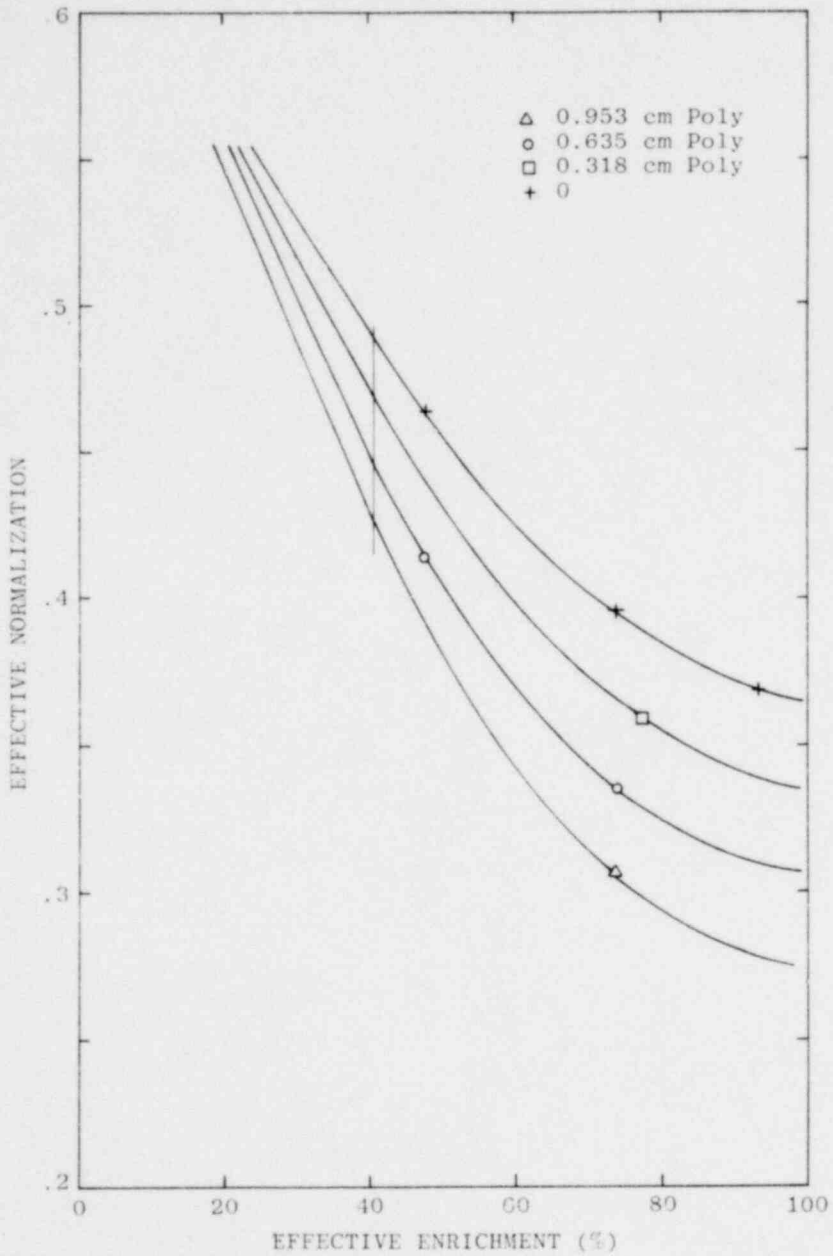

Figure 6. Normalization Factor vs. Enrichment for Various Polyethylene Thicknesses.

1361 137

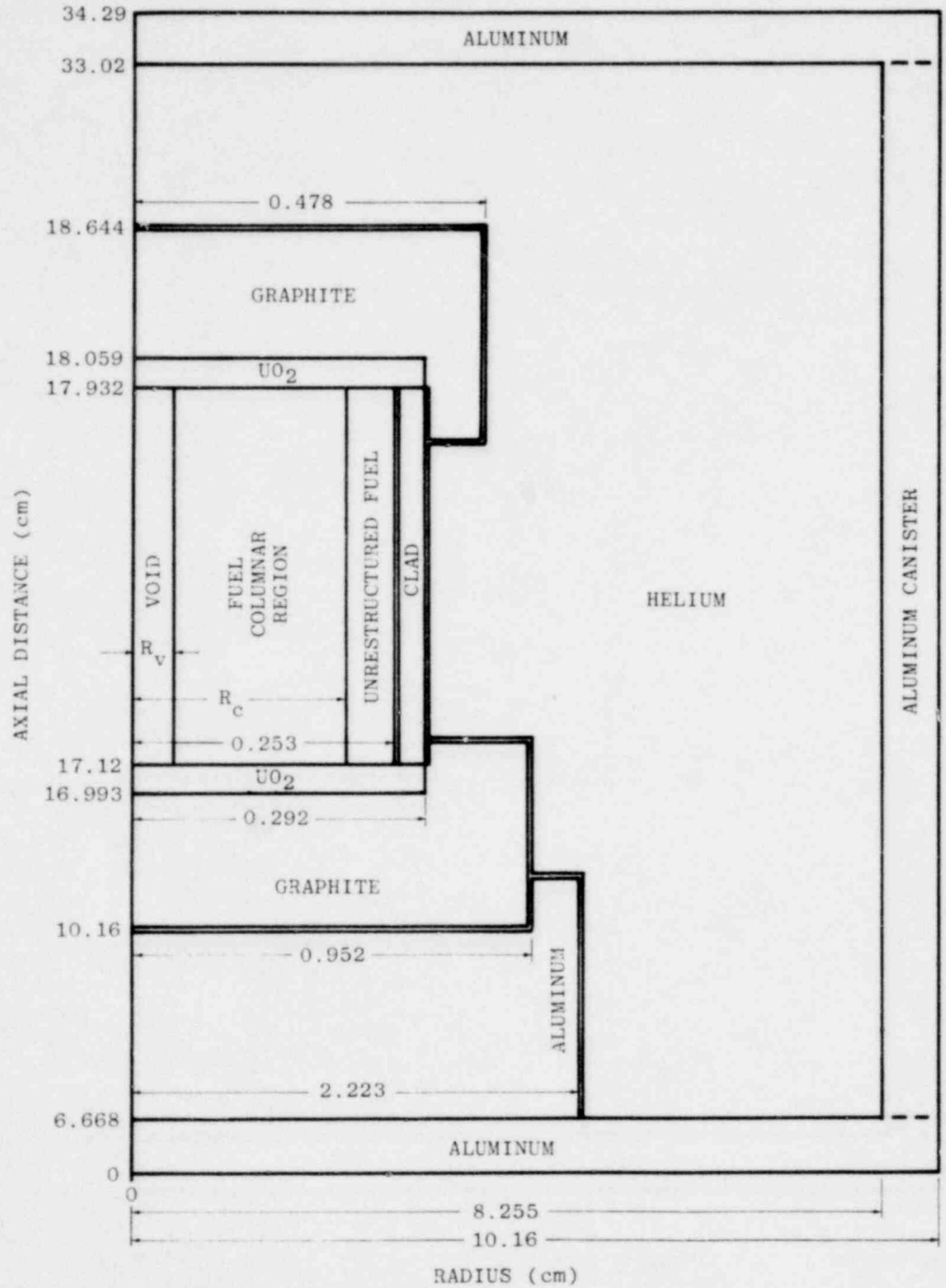

Figure 7. Heat Transfer Model

1361 138

Heat of fusion was included in the fuel but not in the clad for the initial calculations. The melt temperature used for the fuel was 3020 K and for the SS 316 cladding, 1700 K.

A typical calculation is shown in Figure 8. This gives fuel centerline, surface, and clad midpoint temperatures for 78% effective enrichment and an 18/18/18 MJ triple pulse from the ACPR. The clad midpoint goes through its solidus at 2 s, approximately midway between the second and third pulses. Fuel melting temperature is reached on the pellet centerline at 3.2 s, 0.6 s after the third pulse. At this time, the fuel radial temperature profile is prototypic[10] with a ΔT of 490 K, centerline to surface. Results for a 30/12 MJ and a 50/30 MJ double pulse in 78% and 48% enriched fuel, respectively are given in Figures 9 and 10. The double pulse at higher enrichments (one second between pulses) did not allow time for the clad to melt off before the second pulse arrived. In addition, the radial flux profile is highly inverted.

On the basis of the combined calculations, it was decided to use 0.635 cm of moderator on the PNL 9-44 pellets (48% effective enrichment, as fabricated) and 0.318 cm on the higher enrichment pellets (78% effective enrichment, as fabricated). The triple pulse operating mode with 0.25 s to 1.0 s between pulses was picked to yield the best radial temperature profile and to allow the clad to melt before the final pulse.

3.3.4 Dosimetry

Pretest dosimetry with 70% enriched UO_2 pellets indicated close agreement (~3%) with TWOTRAN energy deposition results for the no-moderator case. Dosimetry on pellets with moderator was 20% higher than TWOTRAN. Dosimetry using aluminum wire loaded with 1.0 weight percent 93% enriched uranium metal gave high results due to the lack of self-shielding. The aluminum wire dosimetry was regarded as very inconclusive due to the presence of high axial and radial peaking factors in the actual pellet, which make it difficult to relate the wire energy deposition to either a surface or an average deposition in the pellet.

For the mixed oxides, actual effective enrichments later were found to be lower (40% and 68% after burnup) than originally used in the pre-test calculations (48% and 78% as fabricated). This required using up to 0.953 cm polyethylene moderator.

3.4 FD-1 Tests - Data and Results

In addition to utilizing fuels of a variety of parameter values, the different pellets were exposed to a diversity of experiment conditions. The latter are listed in Table 3 alongside each individual test and pin of origin. Figures 11 and 12 depict the power multipulse and energy generation histories of events FD 1.4 and 1.6, respectively. The calculated average energy density produced in the fuel and fuel average temperature-rise rate per pulse is depicted, without losses, in Figure 13. Corresponding temperature histories of different regions of a given fuel pellet were shown in Section 3.3. These figures serve to typify the 12 experiments.

The motion picture technique proved to be an eminently suitable method for this type of study. Photographic records were obtained for all the experiments

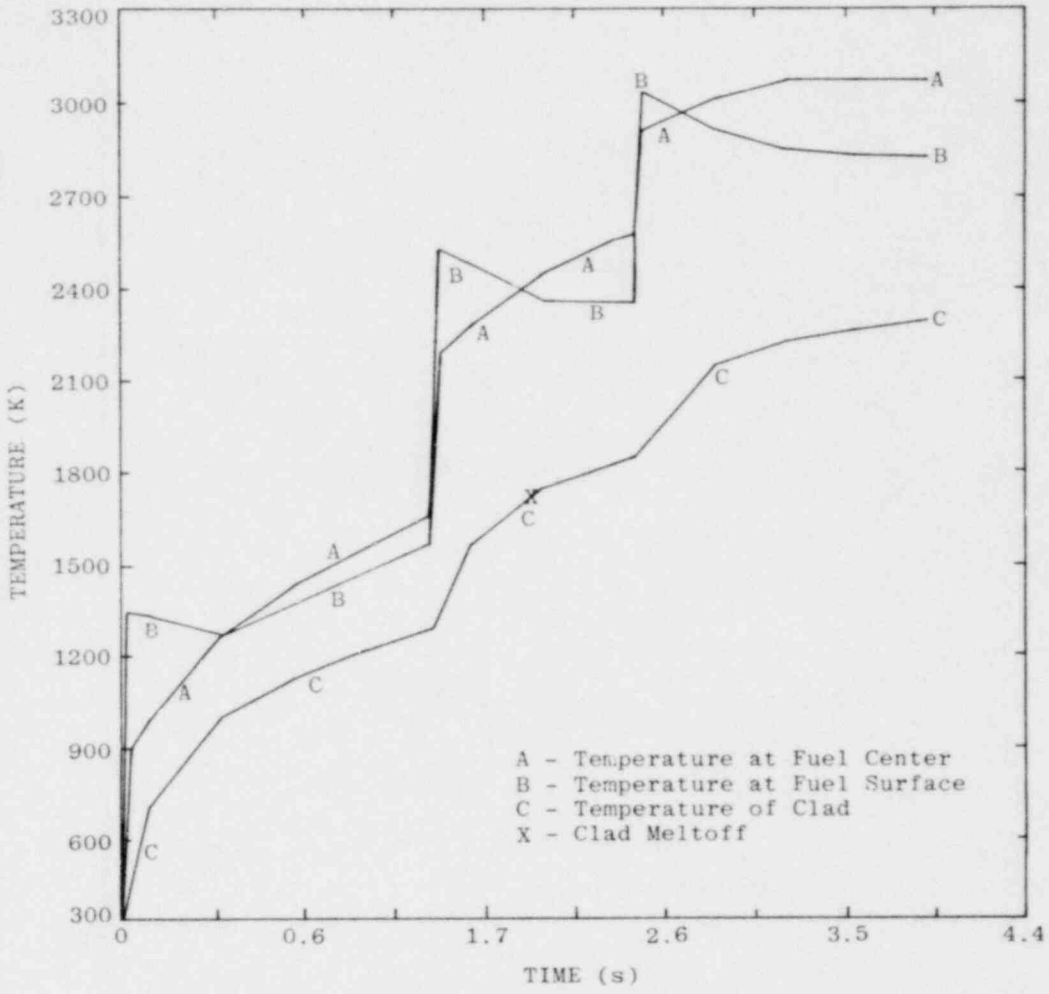

Figure 8. Triple Pulse, 18/18/18 MJ (Excluding 10 MJ in each Pulse Tail), 78% ^{235}U in U, no Moderator.

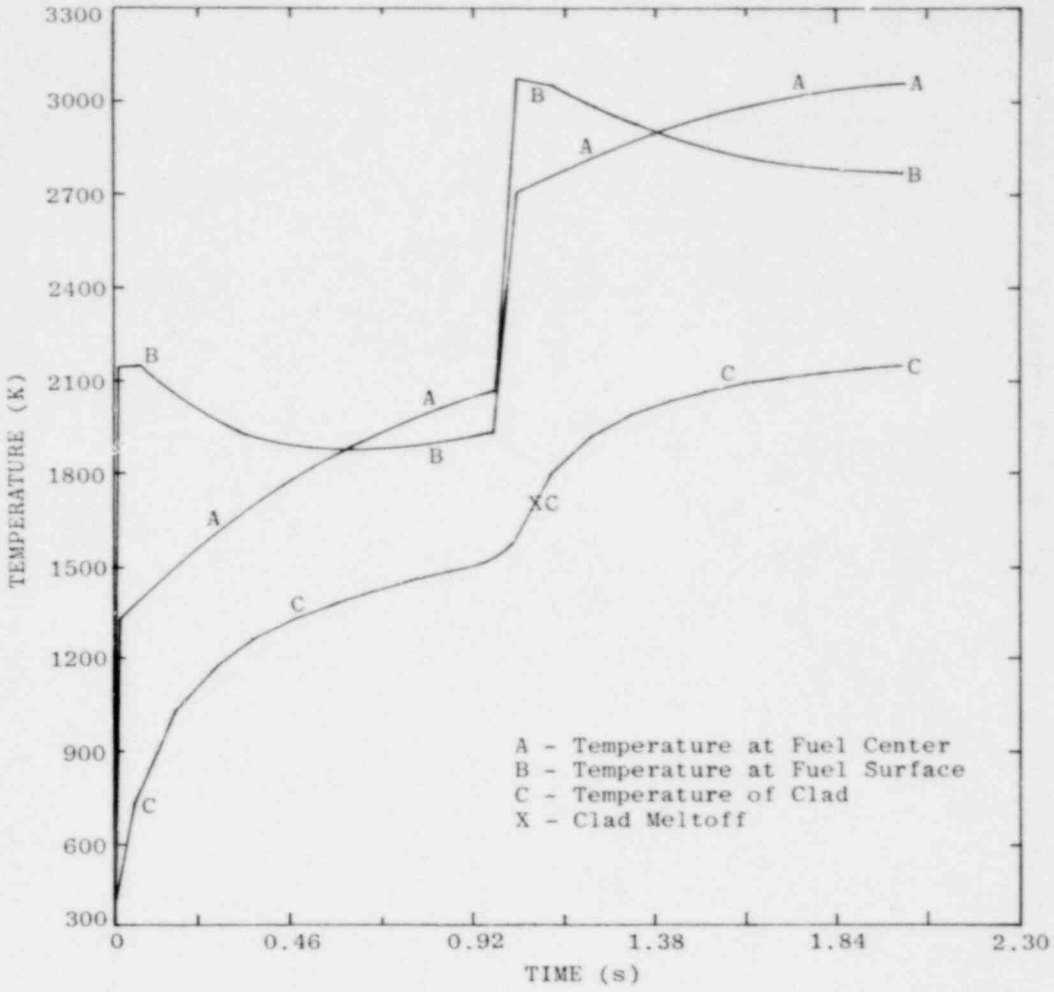

Figure 9. Double Pulse, 30/12 MJ (Excluding 10 MJ in each Pulse Tail), 78% ^{235}U in U, no Moderator.

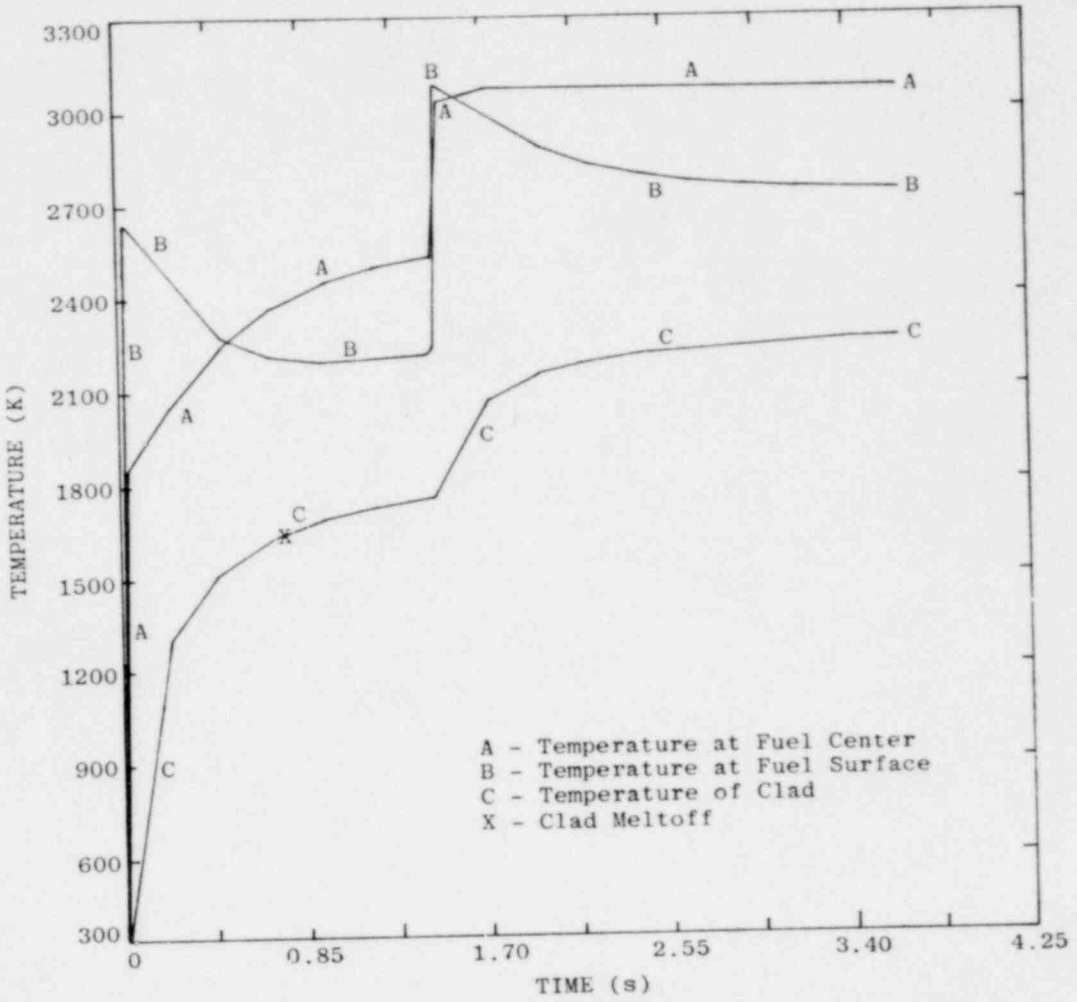

Figure 10. Double Pulse, 50/30 MJ (Excluding 10 MJ in each Pulse Tail), 48% ^{235}U in U, no Moderator.

Table 3. FD-1 Experiments Parameter Values

PNL Pin No.	Test No.	Time Between Neutron Pulses (s)	Moderator Thickness (cm)	$E_{p/m}$ Radial	$E_{p/m}$ Axial	Film Framing Rate at FPP* (per s)	ACPR E total (MJ)
9-44	6 (2 pulses)	.45	0.635	2.68	2.28	2000	83.5
e = 40.5%	10	.25/.24	0.953	2.82	2.41	2250	73.1
	11	.50/.26	0.953	2.82	2.41	1360	72.6
10-12	1	.33/1.05	0	3.07	2.42	450	70.2
e = 67.1	2	.33/1.05	0.318	3.32	2.60	500	68.3
	5	.42/.51	0.953	4.02	3.01	1000	74.0
	7	.77/1.01	0.953	4.02	3.01	1025	69.0
11-18	3 (2 pulses)	.44	0	3.10	2.44	450	87.5
e = 67.7	4	.91/.99	0.953	4.05	3.10	1000	69.1
	8	.75/.74	0.953	4.05	3.10	1000	70.3
Fresh Fuel	9	.41/.51	0.953	4.15	3.15	1000	73.2
e = 70.0	12 (2 pulses)	.46	0	3.15	2.45	2150	87.5

* Final Pulse Peak

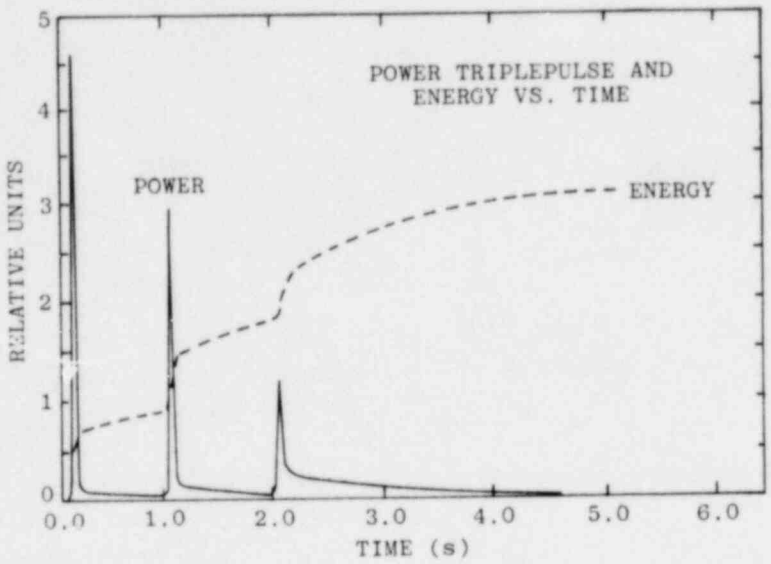

Figure 11. FD 1.4 Power Pulse and Energy History, ACPR and Fuel.

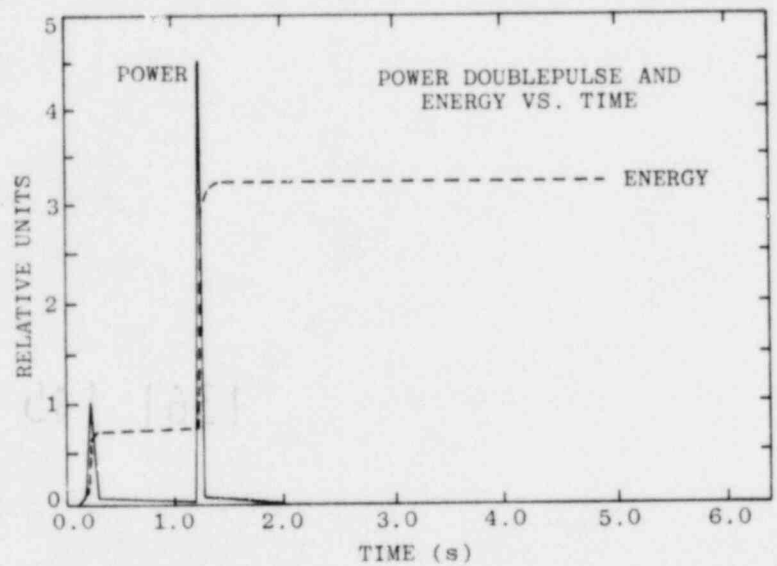

Figure 12. FD 1.6 Power Pulse and Energy History, ACPR and Fuel.

1361 144

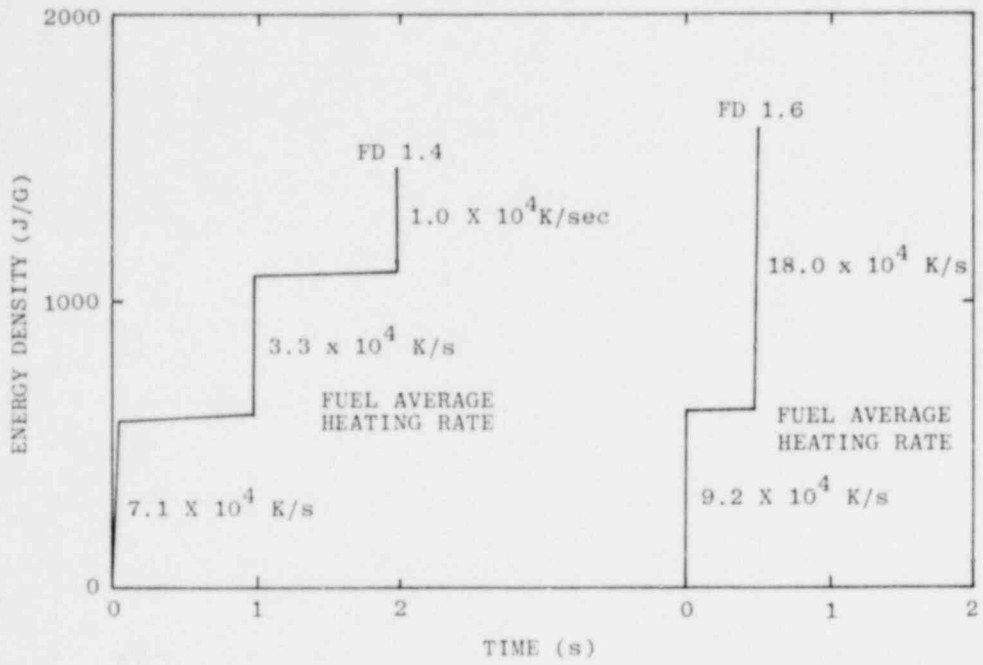

Figure 13. Calculated Average Energy Density Generated in Fuel vs. Time.

1361 145

in this first series. Fuel failure modes were recorded ranging from moderate swelling to rapid fuel dispersal for the preirradiated fuel, and clad melt with no fuel disruption to fuel dispersal for the fresh UO_2. By varying the pulse timescales, fuel surface temperatures ranging from 2450 K to 3500 K were achieved in the various experiments. The fuel's surface temperature and (in the tests in which the fuel cracked but did not otherwise disrupt) inner temperatures were determined by means of photographic radiometry. The calculated fuel surface temperatures, as discussed in Section 3.3, were within the ±5% uncertainty of the average values obtained from the films. Swelling rates and amounts, dispersal velocities and approximate, localized internal pressures in some tests were determined from the film record. There was total absence of molten-steel-clad wetting of the fresh UO_2 and preirradiated mixed oxide.

Table 4 is a brief summary of the experimental results, but it only superficially describes the effects. The motion picture films show the action on the time scale of a fraction of a millisecond for the duration of each experiment. The response of the fuel to each pulse of neutrons and the concomitant behavior of the clad are shown clearly. In several experiments, emanation and escape of gaseous material is seen to occur as a result of the first two pulses in a triple-pulse and prior to clad rupture. Details of the latter process together with clad peel and melt, and fuel swelling are vivid and distinct. This is illustrated by four frames of FD 1.7 shown in Figure 14. Note the non-wetting drop of molten clad resting against the pellet at time t_4. Tests FD 1.1-1.3 were for diagnostics and calibration only. They will not be discussed further.

In tests FD 1.4, 1.7 and 1.8 the time interval between pulses was at most 1 s and at least 3/4 s. The mode of pin breakup observed was very rapid swelling commencing on the second pulse for 1.4 and 1.7, and on the third pulse for 1.8. The clad bulged, ruptured, peeled and finally melted, thus denuding the swelling fuel which cracked but did not disperse further. Swelling amounts and rates were determined from the film record and are shown in Figure 15. For tests FD 1.4, 1.7 and 1.8, the maximum volumetric swellings were 37%, 55% and 68%, respectively. The swelling was initially very rapid. The times, from the third pulse, for the fuel to reach 2/3 of the final volume increase, were 0.1 s, 0.2 s, and 0.05 s, respectively. The swelling rapidly ended, forming a plateau of little or no further growth despite a constant or slightly increasing calculated temperature.

A discontinuity was observed for FD 1.4 and 1.7 between the swelling data measured from the clad surface and that measured from the fuel surface after clad peeling. It appears that the clad pulled away from the fuel surface between the second and third pulses. The swelling in FD 1.8 occurred so rapidly that it was impossible to tell whether or not the same discontinuity was present in the data. These features, which can be seen in Figure 15, are discussed in the next section.

In tests FD 1.5, 1.10 and 1.11 not enough time was allowed between pulses for sufficient energy loss and temperature relaxation for the fuel or clad to remain intact. Section 3.2 pointed out that the axial and radial peak to minimum (P/M) energy generation ratios in a pulse were as high as 4, depending on the fuel and amount of neutron moderation. This indicates that an outer annulus of fuel at the axial ends of the cylindrical pellets could achieve significantly higher temperature than the rest of the fuel, if for a given amount of energy in a pulse, not

Table 4. Summary of FD-1 Experiments Results

Test	Time Between Pulses	Mode of Clad Disruption	Mode of Fuel Disruption	Surface Avg. Temperature Determined From Film (K)	Time Temperature Determined After FPP* (ms)	Remarks
1	0.33/1.05 s	None	None	---	---	Fuel Response Calibration
2	0.33/1.05	Bulge	None	---	---	" " "
3	0.44	None	End Spray	---	---	" " "
6	0.45	None	End Spray	2700	0	" " "
4	0.91/0.99	Rupture/peel/melt	Swell 37%	2525	60	Basic Test Data
7	0.77/1.01	" " "	Swell 55%	2550	183	" " "
8	0.75/0.74	" " "	Swell 68%	2650	25	" " "
5	0.42/0.51	Tear	Rubble Spray	3300	120	" " "
9	0.41/0.51	Melt	None	2900	135	Fresh Fuel Comparison
12	0.46	None	Melt-Spray	3150	10	" " "
10	0.25/0.24	Rupture/peel/melt	End Spray/Swell	2450	137	Basic Test Data, Too Much Power
11	0.50/0.26	" " "	End Spray/Slump	3200	45	" " "

* Final-Pulse Peak

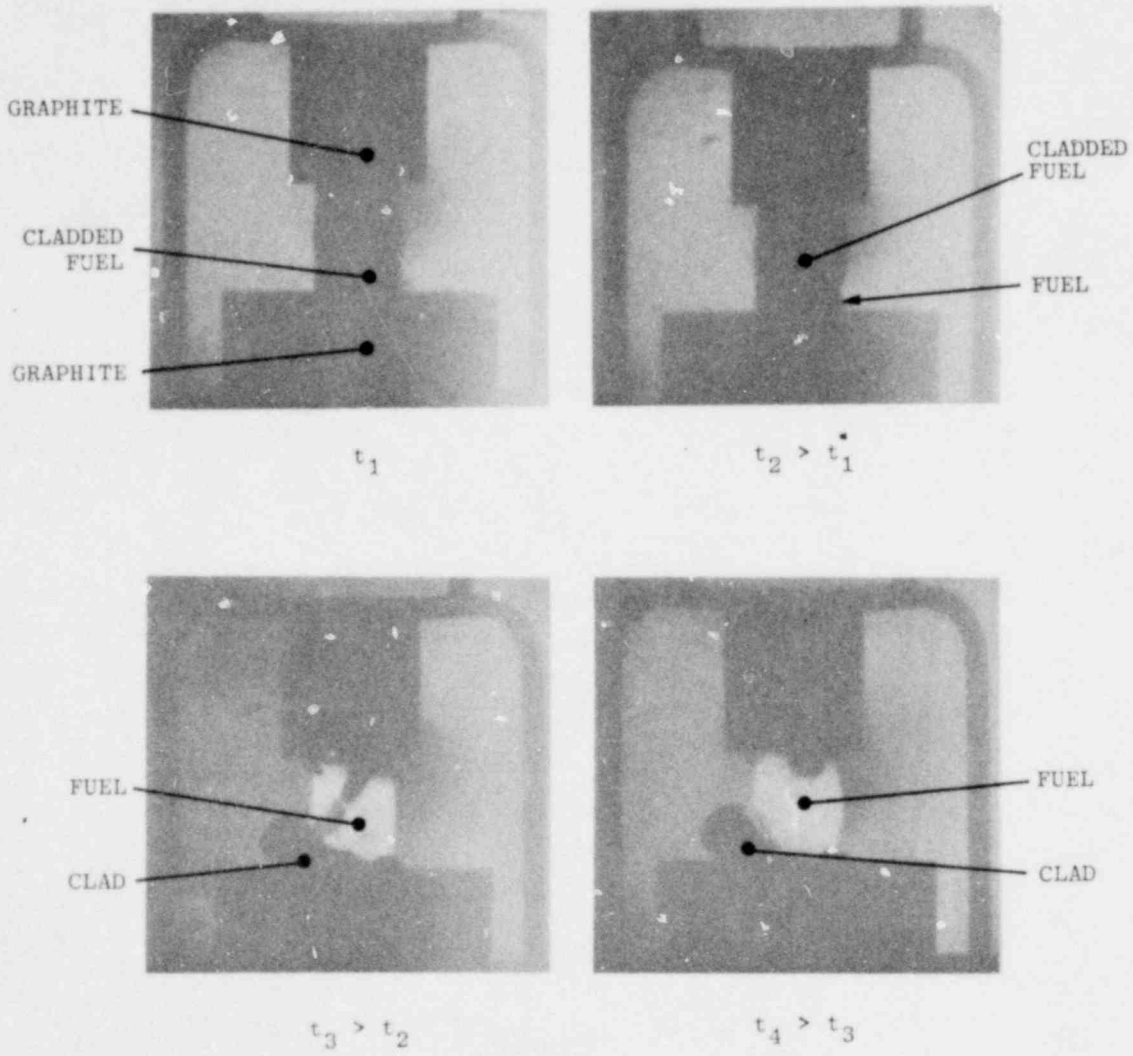

Figure 14. Four Frames from FD 1.7 Film vs. Time, t_4 is end of Test.

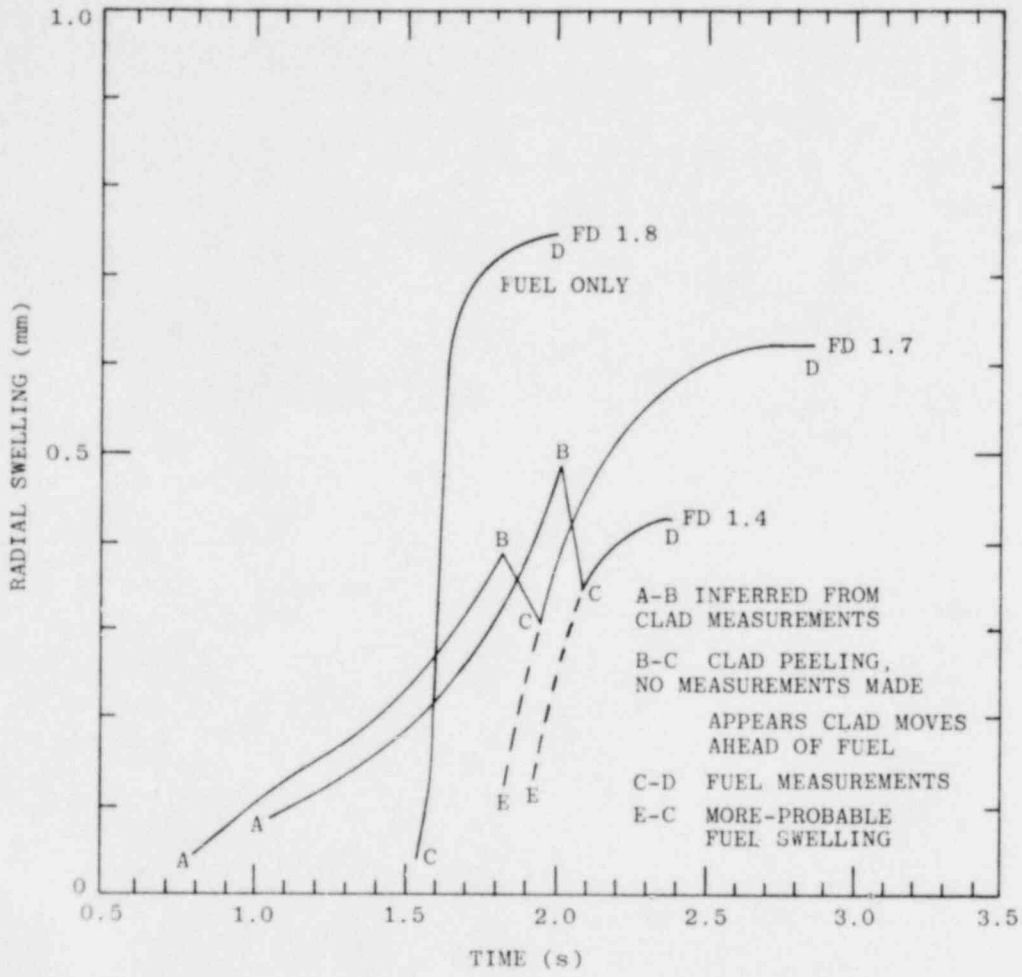

Figure 15. Fuel Swelling in FD1 Tests.

1361 149

enough time is allowed before a subsequent pulse arrives. In this case, occluded fission gases and other fission products which can volatilize at temperatures up to fuel melt (3020 K), could pressurize sufficiently to force molten fuel in the annuli to spray out of the top and bottom junctures of the pellet and graphite holding blocks. For the fuels and ACPR triplepulse energy utilized, it was established experimentally that a pulse interval less than 0.5 s produced this effect.

In the three tests FD 1.5, 1.10 and 1.11 such an internal energy state was just achieved. The highest localized internal energy state reached was in FD 1.5. Here pulse intervals of 0.42 s and 0.51 s and fuel of 67.1% fissile atom enrichment were used. In tests 1.10 and 1.11 the pulse intervals were shorter, but the fuel was only 40% enriched. In all three, some fuel spurted out and the rest proceeded to break up or to slump.

In test FD 1.5, the fuel became so weak after the third pulse that it appeared to be crushed by the spring loaded upper graphite block. The block was accelerated downwards at ≈30g. The fuel was ejected radially: an outer shell of solid fuel was blown apart into fragments of 1 mm or larger; molten fuel squirted out behind the solid fragments. The cladding was torn apart into large pieces which moved out with the fuel. Rapid bending of pieces of cladding demonstrated that the steel was at the melting point. Figure 16 shows 4 frames of FD 1.5.

In FD 1.10 and FD 1.11, extensive spray of fuel from the ends of the pellets was observed. Most of the fuel swelled and cracked following the spray, but it remained essentially intact in FD 1.10. In FD 1.11, most of the fuel barely reached liquidus following the spray; it began to slump, but cooled rapidly and stayed mostly together. Figure 16 is illustrative of these two tests.

It is noted that in none of these six tests, three of which approximated the fuel temperature profiles expected in an LOF sequence (FD 1.4, 1.7 and 1.8), and three of which had a cupped profile during most, if not all of the triplepulse (FD 1.5, 1.10 and 1.11) did the fuel break up into a dustcloud or form a liquid froth.

In the fresh UO_2 fuel experiment, FD 1.9, the power pulse history was essentially identical to that of FD 1.5. However, in FD 1.9 the fuel responded very mildly in comparison to the preirradiated fuel, with no swelling or breakup. The clad began to melt 40 ms after the last pulse peak and slid off the fuel at 140 ms. At that time the fuel temperature was 2900 K ± 250 K. Note that in none of these seven tests, did fresh or preirradiated molten stainless steel clad wet the preirradiated mixed oxide, or fresh UO_2 fuel. Also, it did not mix with the molten fuel in FD 1.11. These results question those clad motion models which assume that fuel is well wet by molten steel and that steel remains as an annular film on the fuel pin.

Finally, for the last two tests, FD 1.6 and 1.12, a double pulse was used to achieve the most rapid heating rate in this series. The maximum temperature and pressure again occurred in an outer annulus of each of the fuel axial ends. In FD 1.6 the rate of energy generation and volatilization of occluded fission products caused hot fuel to spray out the ends very rapidly. It is estimated that the localized internal pressure generated was about 0.65 MPa and produced a fuel debris acceleration of about 2500 g. This was estimated by use of early time fuel velocities determined from the film. The expansion velocity 1 ms from start of fuel ejection was 20 m/s.

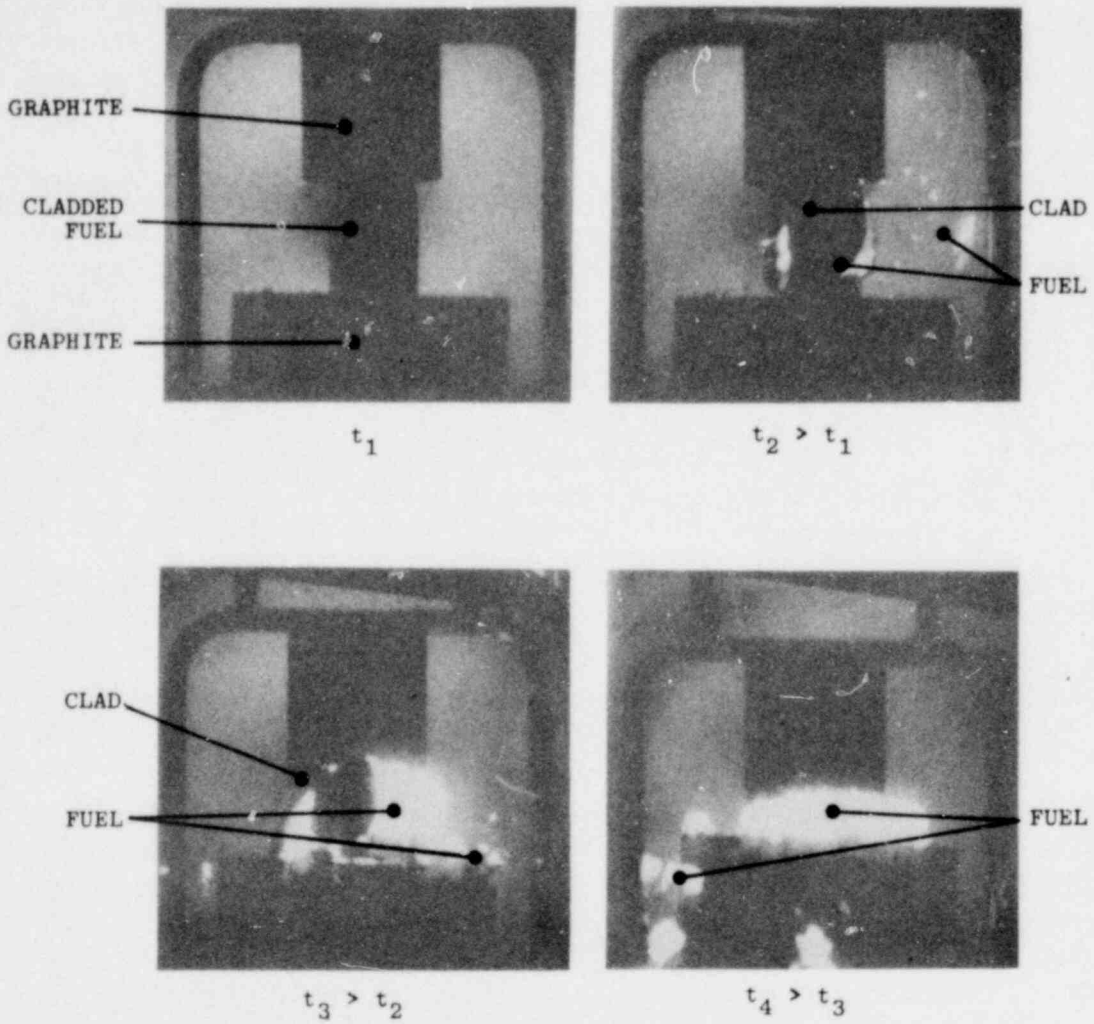

Figure 16. Four Frames from FD 1.5 Film vs. Time, t_4 is end of Test.

The last test in this sequence, FD 1.12, used fresh UO_2 fuel, again for comparison of response with the preirradiated fuel of Test 1.6. The power histories of these two were identical. The fuel behavior was similar, but 1.12 was very mild in comparison to 1.6. In 1.12, very little fuel squirted out, only at the top end, and with much lower velocity than in 1.6. Most of the fuel that came out oozed down the clad outer surface in a molten state and barely managed to drape over it before solidifying. This difference in behavior once more is due to the difference in fission product accumulation and pressurization. Note that in neither case did the clad rupture or melt. The fuel reached melt temperature, but not enough energy was transferred to the clad during the transient to produce melt. Upon fuel spray, the high temperature and pressure were relieved rapidly and the clad remained intact in both cases.

3.5 Posttest Thermal Analysis

3.5.1 Introduction

Posttest thermal analysis was done using the actual reactor power histories and dosimetry results. The model, Figure 7, was altered to include UO_2/PuO_2 properties, heat of fusion in the clad, porosity variations and a central void (if present). A clad peel model also was included and took effect at the experimentally observed time of clad peeloff. The major uncertainties in these calculations were the average energy deposition from dosimetry (±10%) and the gap conductance. By shifting either the gap conductance or the energy deposition over reasonable ranges, variations of several hundred kelvin could be induced in both the fuel surface temperature and clad temperature. Although a nominal value of 3 W/cm^2K was assumed for the gap conductance, this actually could vary from about 0.5 W/cm^2K initially to over 8 W/cm^2K assuming direct mechanical fuel-clad contact.

An additional, unforeseen factor was the observed clad ballooning, as seen in the clad-fuel swelling measurements. This ballooning could be part of the explanation for the observed late clad meltoff. As noted in the Pretest Analysis section (Section 3.3), it was intended to melt off the clad before the last pulse, to give a clear view of the fuel. The experimental result of clad melting shortly after or during the last pulse can be attributed to uncertainties in energy deposition, somewhat lower effective enrichment than originally assumed, and the above-mentioned clad ballooning.

Figures 17-20 give results of heat transfer calculations for tests FD 1.4, 1.5, 1.7 and 1.8. These graphs show fuel center and surface temperatures at the axial midplane of the pellet. Surface temperatures are given with intact clad and with clad removed at the experimentally observed clad-peeloff time. Also plotted are fuel surface temperatures obtained by film densitometry performed on selected frames of the movie film.

Following the third pulse, FD 1.4, 1.7 and 1.8 had a temperature drop of 300-400 K from fuel center to edge (with the clad removed). Clad removal results in a jump of 500 to 600 K in the fuel surface temperature according to calculations; the clad thus acts as a heat sink while it remains on the pellet, helping to establish a prototypic temperature profile.

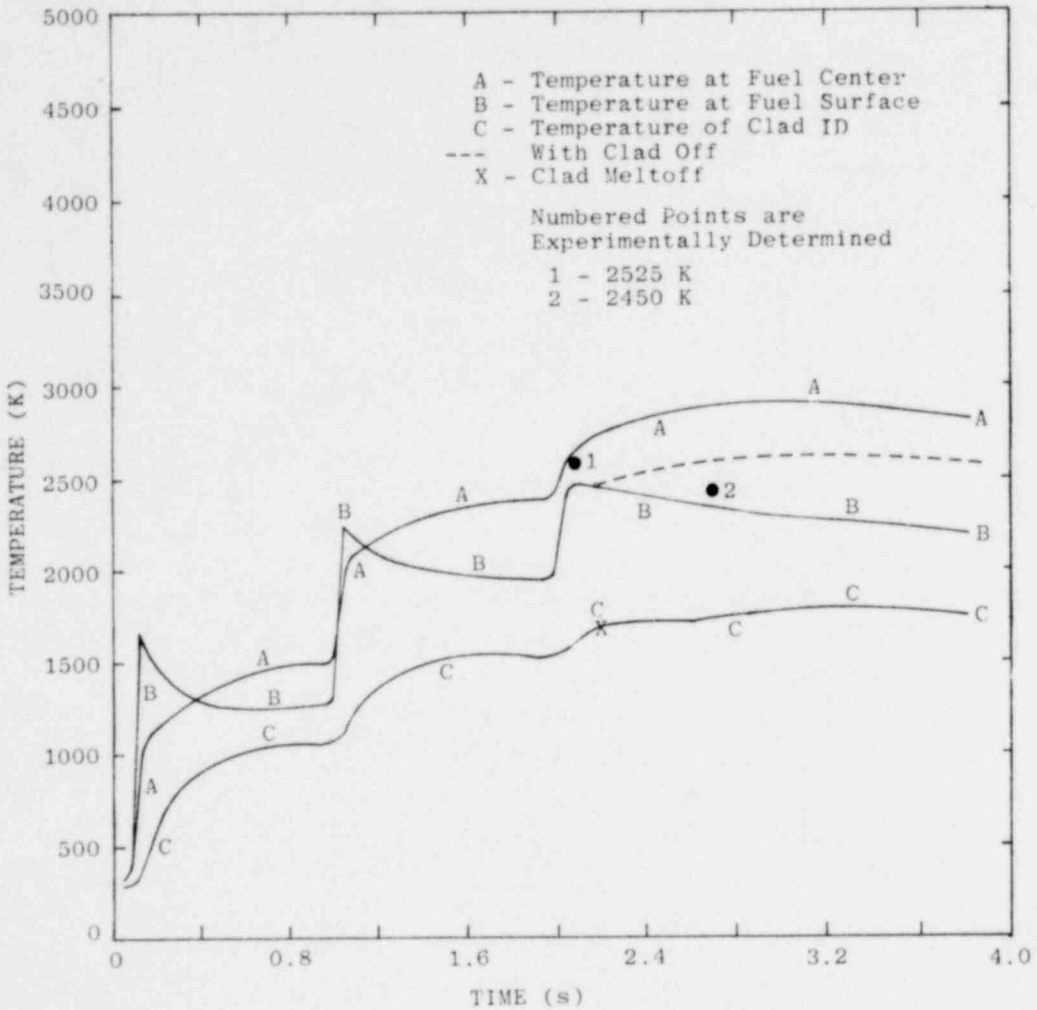

Figure 17. Temperature Histories for Test FD 1.4, PNL 11.

1361 153

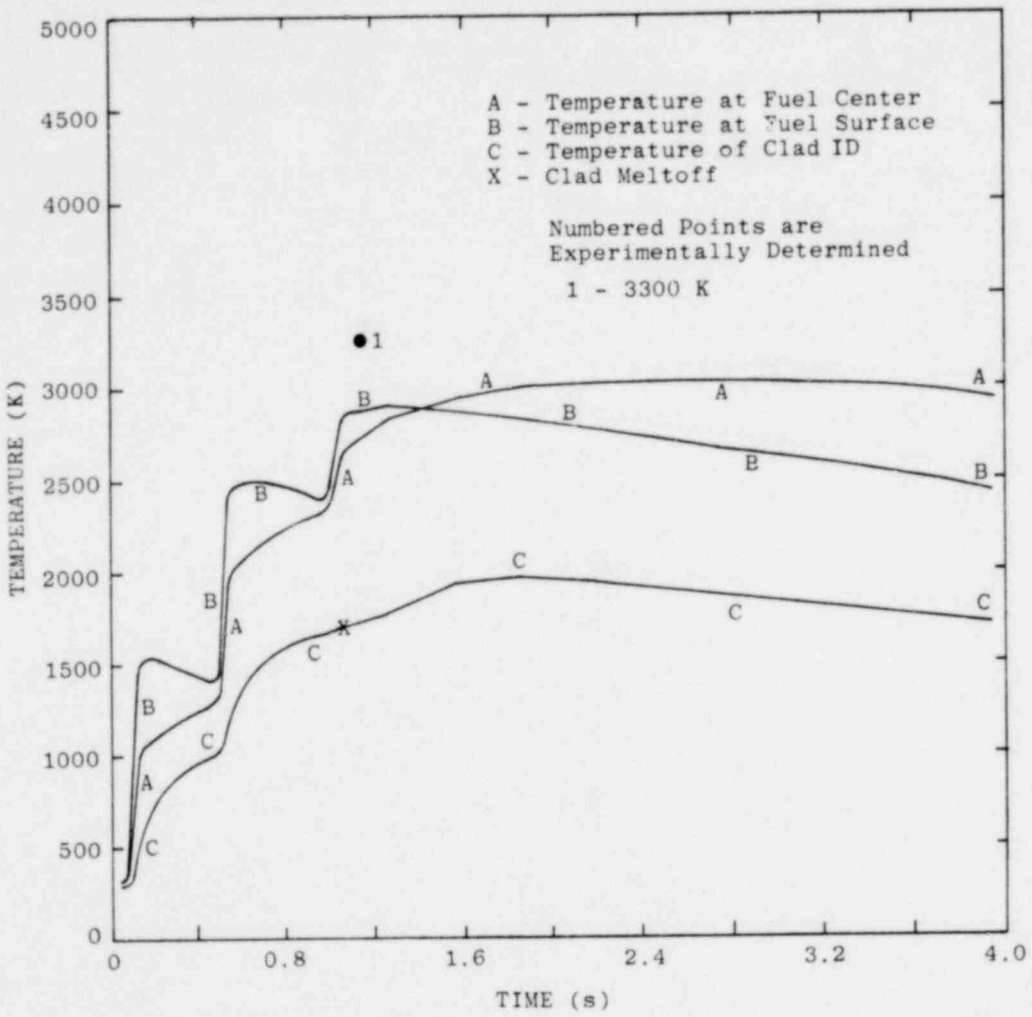

Figure 18. Temperature Histories for Test FD 1.5, PNL 10.

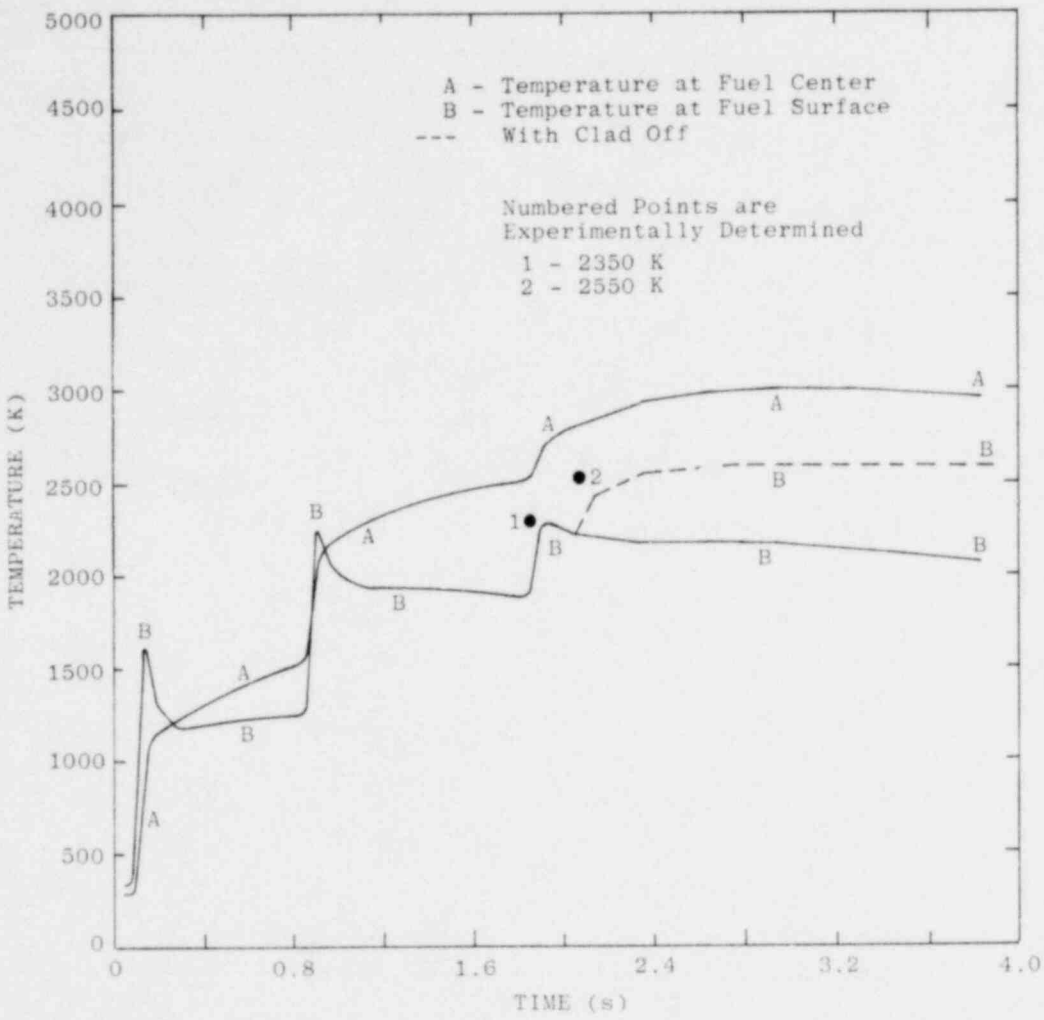

Figure 19. Temperature Histories for Test FD 1.7, PNL 10.

1361 155

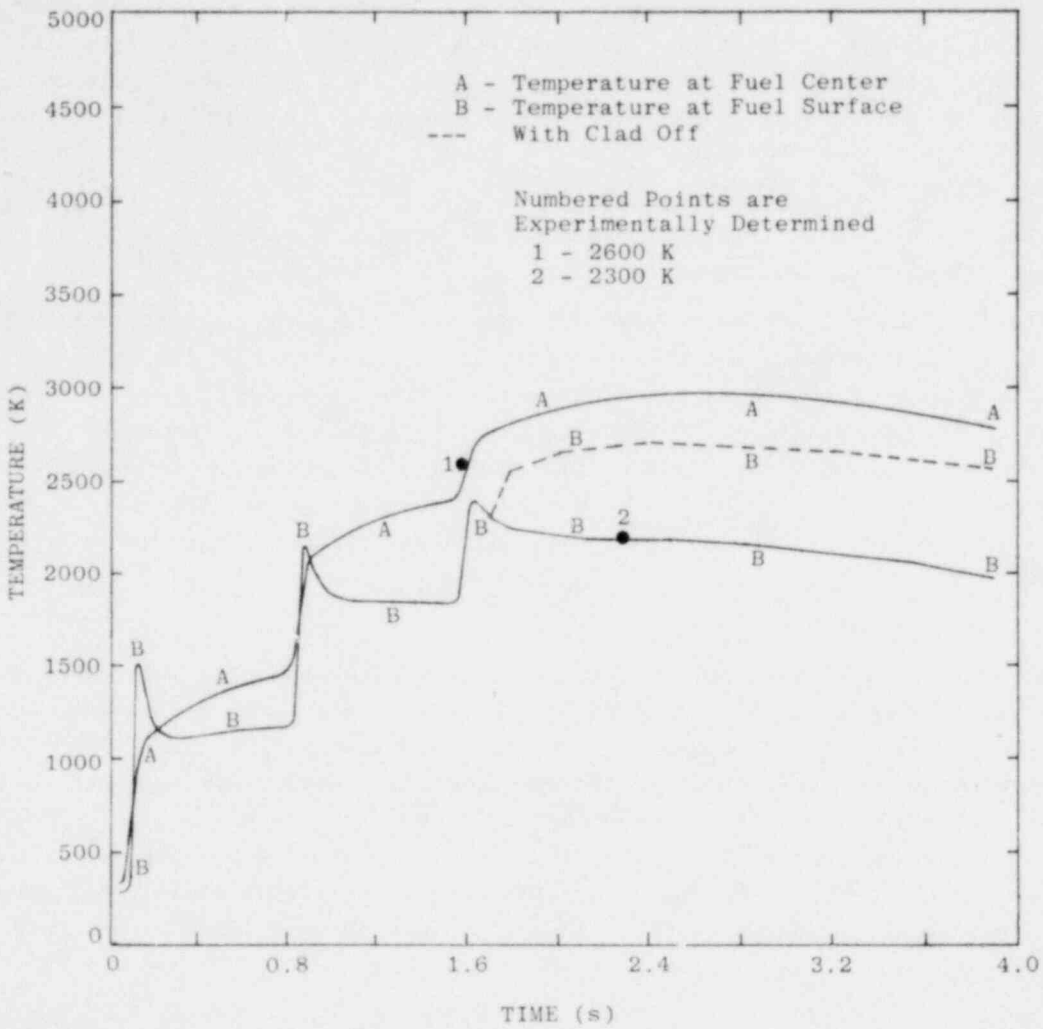

Figure 20: Temperature Histories for Test FD 1.8, PNL 11.

1361 156

FD 1.4 and 1.7 exhibited clad ballooning while FD 1.8 did not. Observing the experiment temperature points in the figures, experimental points taken before 80% clad peeloff are about 100-200 K higher than calculated, while values after 80% clad peeloff are lower than calculated by 150 K (FD 1.4) to 500 K (FD 1.8). The exception to this, FD 1.7, has its second experimental point in the vicinity of the clad peeloff time and thus the measured temperature may not be typical of total (>80%) clad removal. The general trend before 80% clad peeloff is lower predicted fuel temperatures, possibly due to low assumed energy deposition values (by 7-10%) and/or uncertainties in the gap conductance. The predicted temperatures after clad peeloff are generally higher.

The FD 1.5 - experiment fuel dispersed at 1.0 s, the time for which the experiment temperature was determined.

Plots of the calculated temperature profiles across the pellet midplanes in tests FD 1.4, 1.7 and 1.8 are shown in Figures 21, 22, and 23. The data used for these figures are given in Tables 5, 6, and 7. These particular results are based on a more accurate power calibration factor, 15% higher, and a lower gap conductance than that used for Figures 17 through 20. The constant temperature region at a given time at the radial center of the fuel pellet represents the central void region of the fuel pin. The evidence indicates T_{melt} was not exceeded.

3.5.2 Clad Ballooning

Several possibilities were investigated to explain the observed ballooning of clad away from the fuel. These included bowing due to a thermal gradient, compression by the spring-loaded end cap, and internal gas pressure. The general conclusion from considering all three possibilities is that the clad is at or near its solidus (1700 K), or some 100-200 K hotter than calculated. The only significant thermal gradient is axial and amounts to about 600 K, clad midplane to end. This did not introduce any measurable bowing other than could be attributed to simple thermal expansion of the clad. This is 0.09 mm at 1700 K, or about 25% of the observed ballooning.

The maximum axial load on the clad was estimated to be 4.25 N, 1.47 N from the weight of the cap and 2.78 N (10 oz) from the compression springs used to hold the cap in place. The effect of both the axial load and the thermal stress was modeled with a two-dimensional finite element code, SASL.[23] The axial load did not produce any measurable bowing. It should be noted that the axial load is two orders of magnitude below the critical load for buckling at 1500 K (highest temperature for which a value for Young's modulus could be obtained), indicating higher clad temperatures. The absence of many small waves in the clad as in typical buckling also suggests that either the axial load is not the primary cause of ballooning or that internal gas pressure is damping the waves.

The final possibility investigated to explain the observed clad ballooning was that of internal gas pressure. Based on the maximum axial load and the internal area of the end cap, a value of 0.2 MPa pressure differential is required to lift it. If only the gap area is available for gas pressure to act upon, this value goes up to 3.6 MPa. Disregarding the possibility of the end cap and clad

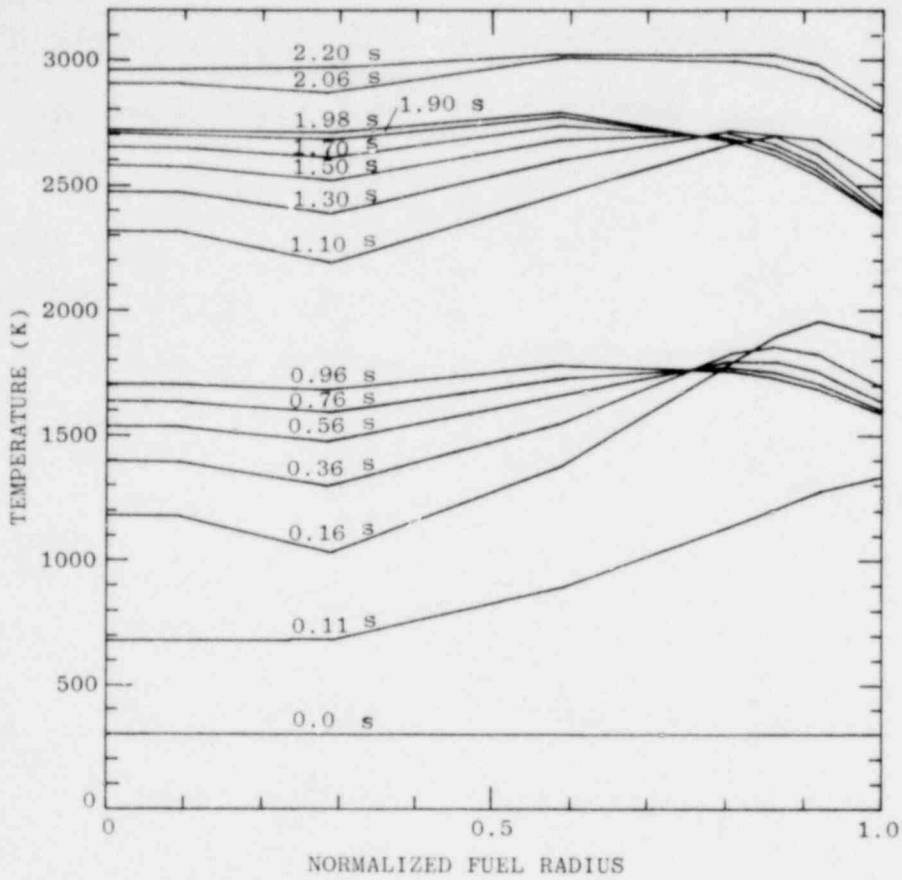

Figure 21. Temperature Profiles in Test FD 1.4 as Function of Time.

1361 158

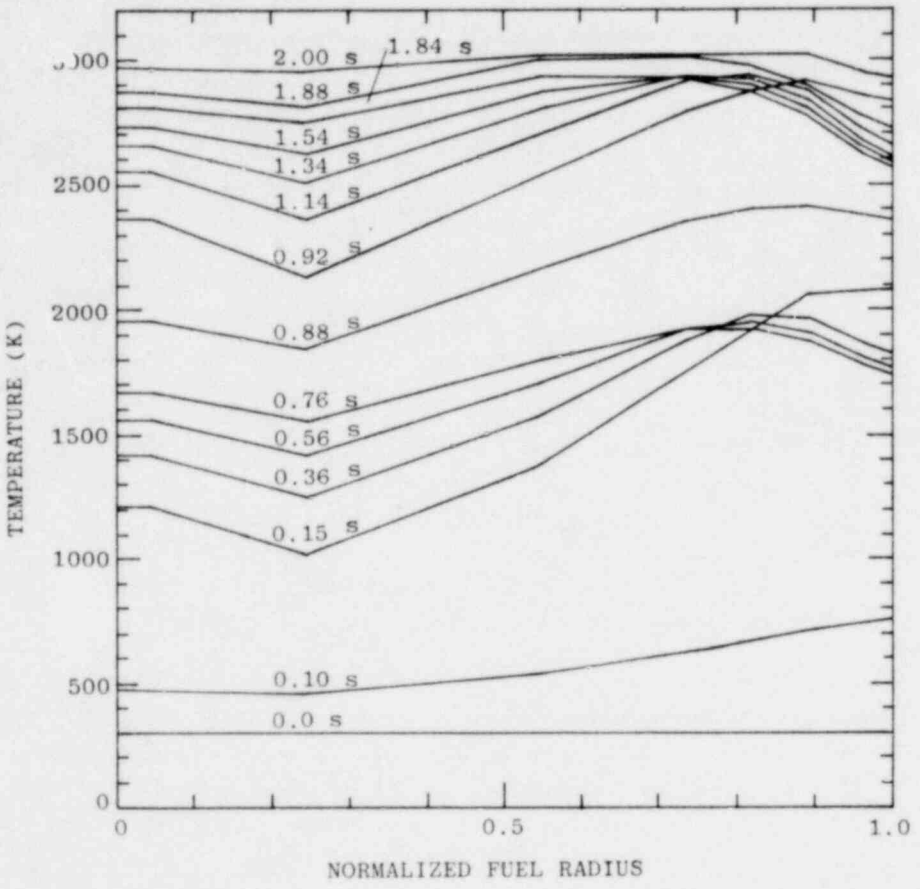

Figure 22. Temperature Profiles in Test FD 1.7 as Function of Time.

1361 159

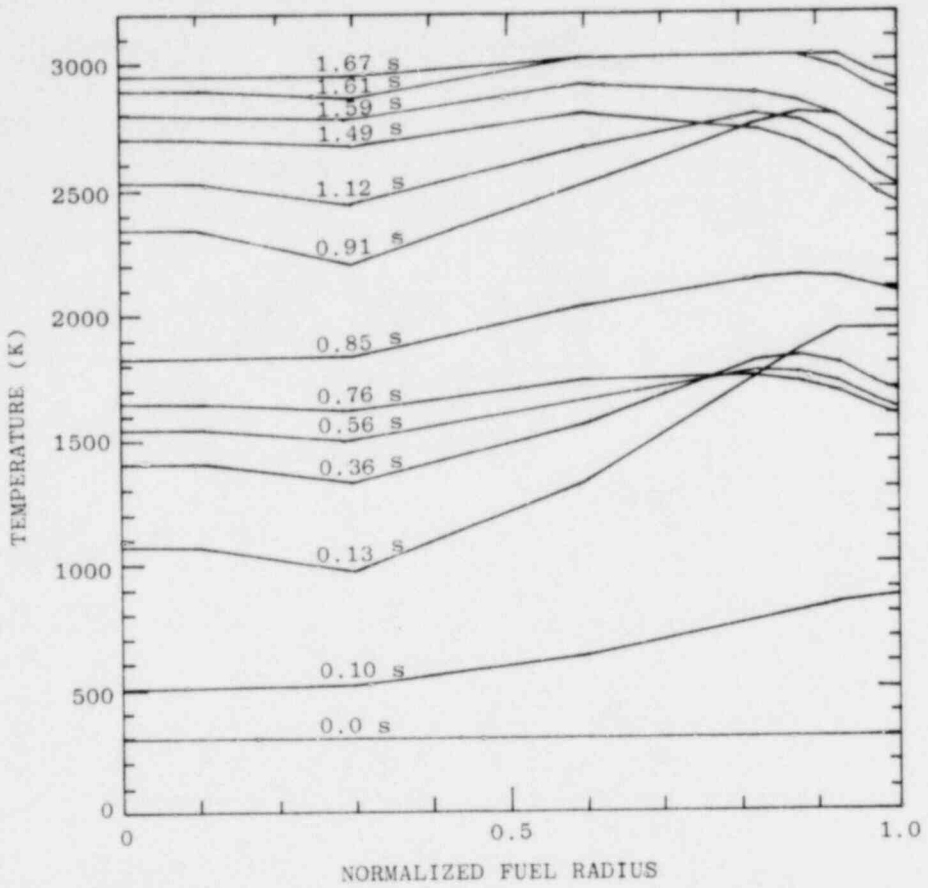

Figure 23. Temperature Profiles in Test FD 1.8 as a Function of Time.

1361 160

Table 5. Temperature Profiles in FD 1.4 as function of time

Normalized Radius =	0	0.091	0.291	0.588	0.806	0.864	0.919	0.973	1.0
Time, s	Temperature, K								
0.0	300	300	300	300	300	300	300	300	300
0.16	1176	1176	1028	1371	1786	1894	1953	1915	1896
0.36	1392	1392	1295	1545	1824	1851	1821	1736	1694
0.56	1532	1532	1470	1657	1792	1789	1748	1670	1631
0.76	1630	1630	1591	1728	1766	1948	1703	1633	1598
0.96	1702	1702	1680	1778	1756	1728	1682	1617	1584
1.1	2317	2317	2191	2464	2664	2695	2679	2575	2523
1.3	2474	2474	2387	2598	2716	2695	2622	2488	2421
1.5	2577	2577	2520	2682	2703	2664	2583	2457	2394
1.7	2651	2651	2616	2738	2688	2639	2556	2438	2379
1.9	2704	2704	2686	2776	2677	2620	2537	2425	2369

Table 6. Temperature Profiles in FD 1.7 as function of time

Normalized Radius =	0.0	0.045	0.245	0.550	0.743	0.823	0.896	0.965	1.0
Time, s	Temperature, K								
0.0	300	300	300	300	300	300	300	300	300
0.1	470	470	455	541	629	670	710	739	754
0.15	1209	1209	1014	1380	1755	1923	2055	2071	2079
0.36	1416	1416	1246	1577	1897	1970	1959	1857	1806
0.56	1557	1557	1415	1707	1919	1944	1902	1800	1749
0.76	1667	1667	1552	1797	1921	1920	1868	1773	1726
0.88	1953	1953	1840	2166	2353	2398	2408	2370	2351
0.92	2363	2363	2130	2534	2791	2870	2910	2850	2820
1.14	2548	2548	2358	2702	2913	2932	2869	2706	2625
1.34	2651	2651	2505	2798	2932	2917	2829	2665	2583
1.54	2725	2725	2618	2863	2929	2893	2797	2641	2563
1.84	2804	2804	2744	2927	2918	2864	2764	2616	2542
1.88	2868	2868	2804	2998	3008	2969	2890	2763	2700
2.00	2966	2966	2955	3020	3020	3020	3020	2951	2917

Table 7. Temperature Profiles in FD 1.8 as function of time

Normalized Radius =	0.0	0.100	0.300	0.598	0.822	0.876	0.926	0.975	1.0
Time, s	Temperature, K								
0.0	300	300	300	300	300	300	300	300	300
0.10	501	501	510	629	768	805	838	858	868
0.13	1071	1071	971	1324	1744	1851	1929	1923	1935
0.36	1403	1403	1323	1554	1810	1827	1795	1716	1677
0.56	1544	1544	1496	1661	1766	1758	1718	1647	1612
0.76.	1645	1645	1617	1734	1745	1724	1681	1616	1584
0.85	1826	1826	1833	2033	2137	2148	2140	2100	2080
0.91	2343	2343	2204	2512	2753	2788	2779	2680	2631
1.12	2529	2529	2443	2661	2785	2762	2686	2551	2484
1.49	2698	2698	2670	2792	2726	2675	2592	2475	2417
1.59	2794	2794	2776	2913	2871	2836	2776	2680	2632
1.61	2893	2893	2860	3020	3020	3017	2974	2885	2841
1.67	2951	2951	2952	3020	3020	3020	3020	2947	2910

sticking or sealing, some pressure is thus available to balloon the clad. For 0.2 MPa, the clad must be at its solidus to yield. For 3.6 MPa, the clad temperature can be as low as 1400 K. An average of the fuel surface and clad temperatures during the time of clad ballooning gives a gas temperature of about 2000 K, or a pressure due to helium only of about 0.2 MPa. The higher pressures thus require some outgassing of the fuel, and if this were the dominant source of gas pressure the total end cap area would certainly be available for gas pressure to act on, again limiting internal pressure to about 0.2 MPa.

3.6 Fuel Swelling Analysis

3.6.1 Qualitative Conclusions

One of the primary purposes of the FD1 test series was to investigate the mode of disruption of irradiated fuel under simulated loss-of-flow conditions. Under the rapid heating conditions present in these tests, fuel was expected to melt and froth, or break up into dust or larger particles. These phenomena were not observed; rapid swelling occurred.

Swelling rates were measured from the film record. Plots of the swelling are shown in Figure 15. Note that no axial motion of the upper end caps occurred for tests FD 1.4, 1.7 and 1.8. Thus, the swelling shown in Figure 15 is in no way due to axial squashing of the fuel pellets, demonstrating that the swelling was caused by significant internal forces leading to dilatation of the fuel.

The maximum volumetric swellings were 37, 55 and 68%, respectively, in tests FD 1.4, 1.7 and 1.8. The times, from the peak of the third pulse, for the fuel to reach 2/3 of the final volume increase were 0.1 s, 0.2 s and 0.05 s, respectively. There are ambiguities in the interpretation of tests 1.4 and 1.7 with respect to the actual fuel swelling prior to peeloff of the cladding. However, in view of the very rapid onset of swelling in test 1.8 at the time of the third pulse, it is reasonable to assume that most of the fuel swelling in the other tests occurred after the start of the third pulse.

This very rapid, massive swelling was unexpected. Such fuel behavior is not modeled in LOF accident analysis codes such as SAS. The significance of this effect is that, in an LOF accident, fuel could swell shut the coolant subchannels between pins. This could significantly reduce the axial fuel dispersal between pins as calculated in the SAS code.

The assumption has been made in the past that fuel swelling would only be of importance for low heating rates. Thus, the massive swelling seen in the FGR tests at HEDL[8] and the DEH tests at ANL[25] have been ascribed to slow heating rates, and at nominal power level or lower.[25] It should be noted that the average heating rates during the Sandia tests were on the order of 5 times the CRBR nominal peak power of 200 W/g. It may be argued that the pulse heating mode was not prototypic of the smooth temperature increase in an LOF. However, a more brittle behavior would be expected in a pulse heated system; the heating rates during the pulses were on the order of 100 times nominal.

Based on the data from these experiments, rapid and massive fuel swelling appears to be the initial mode of fuel disruption in an LOF accident.

3.6.2 FISGAS Calculations

The swelling observed in tests FD 1.4, 1.7 and 1.8 was compared to that predicted by standard models. An early version of the FISGAS code[26] was used to do this.

FISGAS is based on the same physical assumptions with respect to intragranular fission gas bubble migration as the FRAS code.[27] Bubbles are subject to both random migration and biased migration in a temperature gradient, with the mobility being due to surface diffusion of lattice atoms. An asymptotic model of bubble migration and coalescence is used to eliminate the distribution of bubble sizes. Completely independent calculations of migration and coalescence are performed for grain boundary gas and intragranular gas. Grain-boundary gas-bubble migration is driven by the projection of the temperature gradient onto the plane of the grain face on which the bubbles are trapped. The fact that bubbles on the grain faces are migrating in a plane changes the qualitative character of the interaction rate equations. Partly because of this, grain-boundary bubbles grow much larger than intragranular bubbles. The growth of intragranular bubbles is limited by the supply of lattice vacancies, which make the results for intragranular gas approximately the same as FRAS2 code results. Grain-boundary bubble growth, however, is not limited by the intragranular supply of vacancies, which is another reason that grain-boundary bubbles become much larger than intragranular bubbles.

In FISGAS, gas release from the fuel involves a three-step process. First, migration of intragranular gas bubbles leads to release of gas from the interior of the grain to the grain boundary. Those bubbles are then trapped on the grain face and forced to migrate along the plane of the grain face. Gas bubbles which migrate far enough to reach a grain edge (intersection of two grain faces) are then released to and trapped on the grain edge. In addition, when the fractional areal coverage of the grain face by gas bubbles exceeds 0.5, the excess gas immediately percolates to the grain edge due to the formation of a network of interconnected porosity. In FISGAS, most of the gas transfer to the grain edge occurs by percolation rather than bubble migration. Release of gas from the fuel to the ambient is controlled by percolation of interconnected porosity on the grain edges. The onset of such release is determined by the volume fraction of grain edge porosity as specified by percolation theory.

Swelling of the fuel is determined from a one-node calculation of fuel creep, based on the equations for creep of an internally pressurized thin cylinder. The driving force for the creep is the excess internal pressure in the fission gas bubbles. The creep rate of the fuel provides a mechanical restriction on the rate of bubble growth and fuel swelling.

FISGAS has a multiple-node structure in the radial direction. Independent calculations of gas behavior are performed for each node. The separate nodes interact only through the creep field of the fuel. For the calculations reported here, either 3 or 4 nodes were used in the gas-bearing unrestructured region of the fuel.

FISGAS is designed as a research tool with the flexibility to include or exclude various options. Models 1 to 4 exclude grain-boundary gas, and models

5 to 8 include it. Models 2, 4, 6 and 8 include delayed intragranular bubble equilibration due to lattice vacancy supply, while models 1, 3, 5 and 7 assume instantaneous equilibration. Models 3, 4, 7 and 8 include the effect of macroscopic fuel creep on restricting the size of all bubbles. This code flexibility makes it possible to explore the sensitivity of the results to model changes. Note that model 1 (M1) corresponds to FRAS-type modeling, while model 2 (M2) corresponds to FRAS2-type modeling.

These model options are summarized in Table 8. Notice that suffixes T and F are used to designate significant model variations. T designates a factor of 100 increase in the time constant for intragranular bubble equilibration. This is designed to simulate a depletion of vacancies in the lattice. Such a depletion has been modeled in the NEBRAS code[28] and has been shown to be important. The F designates an immediate release of all grain edge gas. In that case, only grain face gas contributes to grain-boundary swelling. The A suffix designates that nodes in which the temperature exceeds the solidus temperature are no longer restricted by creep stress. This leads to sudden swelling when the solidus temperature is attained.

The physical constants used in the swelling calculations are given in Table 9. Most of the values used are based on the recommendations of Gruber.[27] Physical parameters of the test fuel itself (grain radius, fission-gas concentration, and restructuring radius) are discussed in the following paragraphs.

3.6.2.1 Grain Size

There are no published data on the grain size of the test fuel. An average grain radius was determined from photomicrographs of the PNL 10-23 fuel as taken from Reference 29, pE52. A line drawn across the micrograph was used to determine a mean linear intercept distance between grain boundaries of 6.69 μm. This is an average over 57 grains.

For a sphere, the mean chord length, c, (which is the same as the mean linear intercept) is related to the radius by[30]

$$c = 4x \text{ volume/surface area.}$$

This implies that the radius of the sphere is 3/4 of the mean chord length. Then, by assuming that the fuel grains are all spherical, an average grain radius of 5.02 μm is found.

The PNL 11 fuel underwent the same manufacturing procedure as that for PNL 10.[31] Therefore, in the absence of any prior data on PNL 11 fuel, it was assumed to be identical to the PNL 10 fuel and to have a 5 μm grain radius.

3.6.2.2 Fission-gas concentration

The concentration of fission-gas in the fuel grains was estimated by means of the Dutt correlation,[32] viz.,

$$F = \frac{1 - \exp(-4.89 \times 10^{-5} B)}{3.234 \times 10^{-5} B} \exp(0.00241Q),$$

where F is the fraction of gas generated in unrestructured fuel that is retained, B is the local fuel burnup (megawatt-days per metric ton of metal), and Q is the local linear power rating of the fuel pin (kilowatts per meter). Then, by using

Table 8. Effects Included in FISGAS Models

Model	Grain Boundary Gas	Bubble Disequilibrium	Fuel Creep
M1*			
M2**		x	
M3			x
M4		x	x
M5	x		
M6	x	x	
M7	x		x
M8	x	x	x

Suffix

T	Vacancy depletion simulated
F	Immediate release of grain edge
A	Relief of creep restriction on melting
*	Equivalent to FRAS1 code
**	Equivalent to FRAS2 code

Table 9. Physical Parameters Used for Swelling Calculations

Parameter	Value
Heat of transport for surface diffusion	4.63×10^{-12} erg
Atomic volume for uranium in UO_2	4.1×10^{-23} cm^3
Vacancy diffusion coefficient	$2 \exp(-7.67 \times 10^{-12}/kT)$ cm^2/s
Surface diffusion coefficient	$3.5 \times 10^4 \exp(-6.26 \times 10^{-12}/kT)$ cm^2/s
Fuel surface tension	630 dyne/cm
Grain radius	5 μm
Fission gas concentration	1.5×10^{20} atoms/cm^3
Fuel radius	2.5 mm
Restructuring radius	1.97 mm in FD 1.4 1.78 mm in FD 1.7 2.02 mm in FD 1.8

a fuel density of 10.3 gm/cm^3 in a grain, a noble gas production rate of 0.25 atoms per fission, and by setting the approximate conversion of 1 atom % burnup to 10,000 MWD/MTM, the gas concentration, c, in gas atoms/cm^3 is given by

$$c = 1.78 \times 10^{20} \left[1 - \exp(-0.489B)\right] \exp(-0.00241Q),$$

where B is the atom % burnup.

Gas concentrations in the PNL test fuel used in the FD 1 test series were calculated using this equation. The results are given in Table 10. The results are clearly insensitive to small variations in steady state power level and burnup. Since the gas concentration values are all very similar, an average value of 1.5 x 10^{20} atoms per cm^3 was used in all calculations.

3.6.2.3 Restructuring Radius

In all calculations performed here, it was assumed that the gas concentration was uniform in the unrestructured fuel and that all gas was released from restructured fuel. The restructuring radius, R, was estimated from the equation

$$R = 0.25 \left[1 + 2k/h(0.25) - 4\pi k(T_R - T_C)/P\right]^{\frac{1}{2}}$$

where 0.25 mm is the assumed fuel radius, k is the fuel thermal conductivity (taken to be 2 W/m-K), h is the gap conductance (estimated to be 7000 W/m^2-K), T_R is the restructuring temperature (about 1620 K), T_C is the cladding temperature (about 720 K) and P is the linear pin power level (W/m). Table 11 gives the calculated restructuring radius for the fuel in tests FD 1.4, 1.7 and 1.8. In addition, it compares the calculated values with data for PNL 10 fuel (HEDL TME 74-23, pE3). The calculated values agree quite well with the data.

3.6.3 Comparison of Data to Intragranular Swelling Models

The FRAS code[33] has frequently been used for analysis of fission-gas behavior under accident transient conditions. More recently, the FRAS2 code[34] has been used. FRAS2 adds bubble disequilibrium to the FRAS modeling. It is similar to earlier codes developed at UCLA.[35,36] FRAS is equivalent to the M1 option in FISGAS, while FRAS2 is equivalent to the M2 option. More advanced modeling is embodied in the NEBRAS code,[28] which is the most recent UCLA fission-gas work. This code accounts for vacancy depletion in the lattice. This important effect is not included in any of the FRAS codes, or in FISGAS. FISGAS may very crudely simulate it by reducing the bubble equilibration time constant by a factor of 100. Such a code calculation will be designated by a suffix T; M2T is an approximate simulation of a NEBRAS calculation.

Swelling predictions for tests 1.4, 1.7 and 1.8 were performed using models M1, M2, M2T and M3. The physical constants used were as given in Table 9. The M3 calculations were done to determine the importance of creep restraint on fuel swelling. These calculations are compared to the data in Figures 24, 25 and 26.

Clearly, M1 modeling (FRAS code) very seriously overpredicts the observed swelling. This is most dramatic in test 1.8 where no swelling occurred prior to the third pulse; the M1 prediction leads to massive swelling beginning at the second pulse. The discrepancy is serious enough to reject the M1 or FRAS-type modeling as invalid. This conclusion confirms the theoretical work on bubble disequilibrium which has led to the recent development of the NEBRAS, and FRAS2 codes.

Table 10. Gas Concentrations in Unrestructured Region of FD-1 Test Fuel, Based on the Dutt Correlation.

Fuel Pin	Location	S.S. Power Level	Burnup	Gas Concentration
PNL 10	Midplane	8.84 kW/ft, 29.0 kW/m	5.4%	1.54×10^{20} cm^{-3}
	Near axial end	7.96 kW/ft, 26.1 kW/m	4.9%	1.52×10^{20} cm^{-3}
PNL 11	Midplane	11.02 kW/ft, 36.2 kW/m	4.7%	$1.47 \times 10^{20} cm^{-3}$
	Near axial end	9.92 kW/ft, 32.6 kW/m	4.2%	$1.44 \times 10^{20} cm^{-3}$

Table 11. Calculated Restructuring Radius for FD-1 Test Fuel

Test	Test Fuel	Steady State Power Level	R_R Calculated, mm	R_R measured, mm
FD 1.4	PNL 11	10.47 kW/ft, 34.4 kW/m	1.97	-
FD 1.7	PNL 10	8.84 kW/ft, 29.0 kW/m	1.78	1.76, 1.78
FD 1.8	PNL 11	11.02 kW/ft, 36.2 kW/m	2.02	-
-	PNL 10	7.51 kW/ft, 24.7 kW/m	1.52	1.43, 1.58

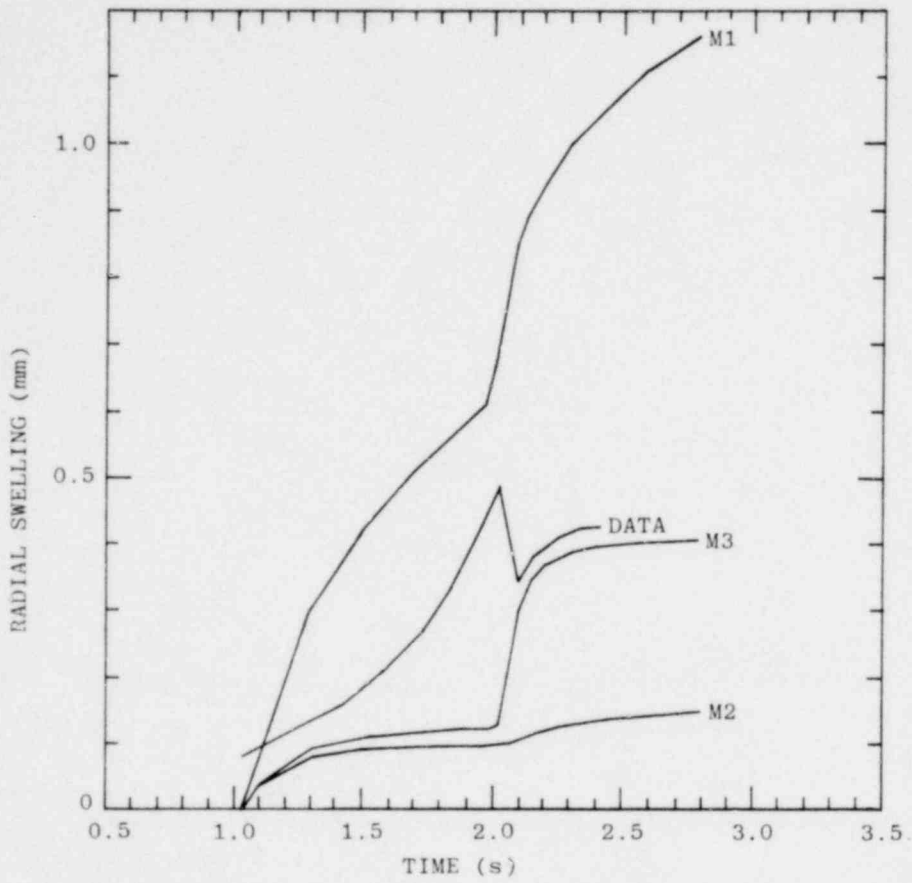

Figure 24. Comparison of FD 1.4 Data to Calculations.

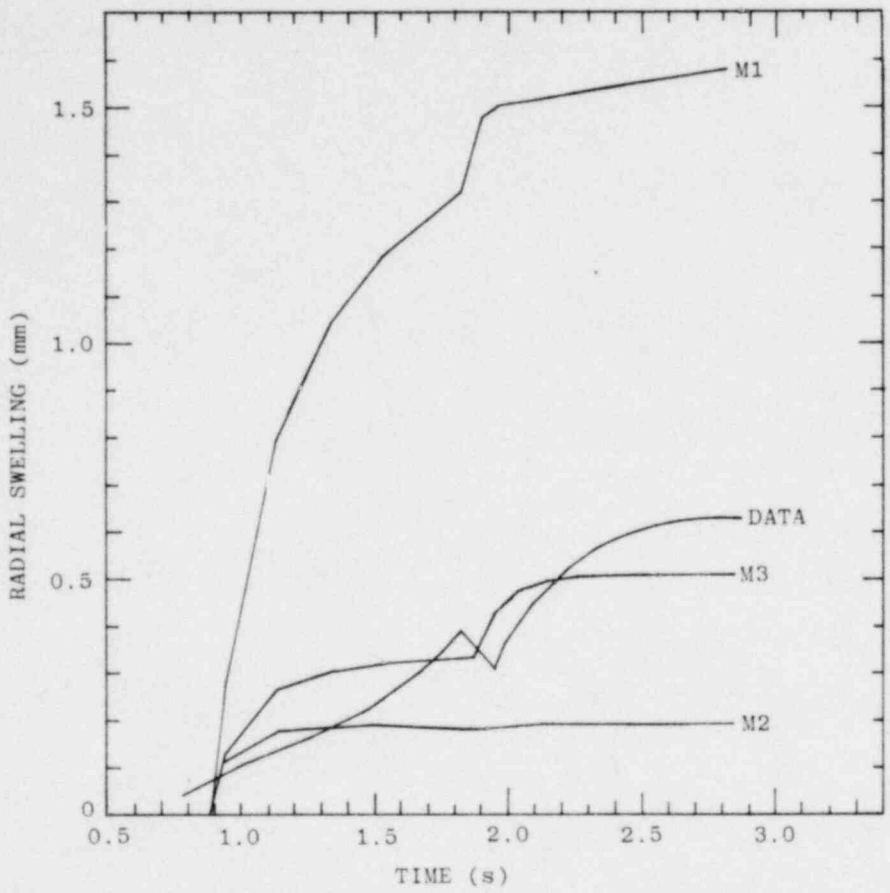

Figure 25. Comparison of FD 1.7 Data to Calculations.

1361 171

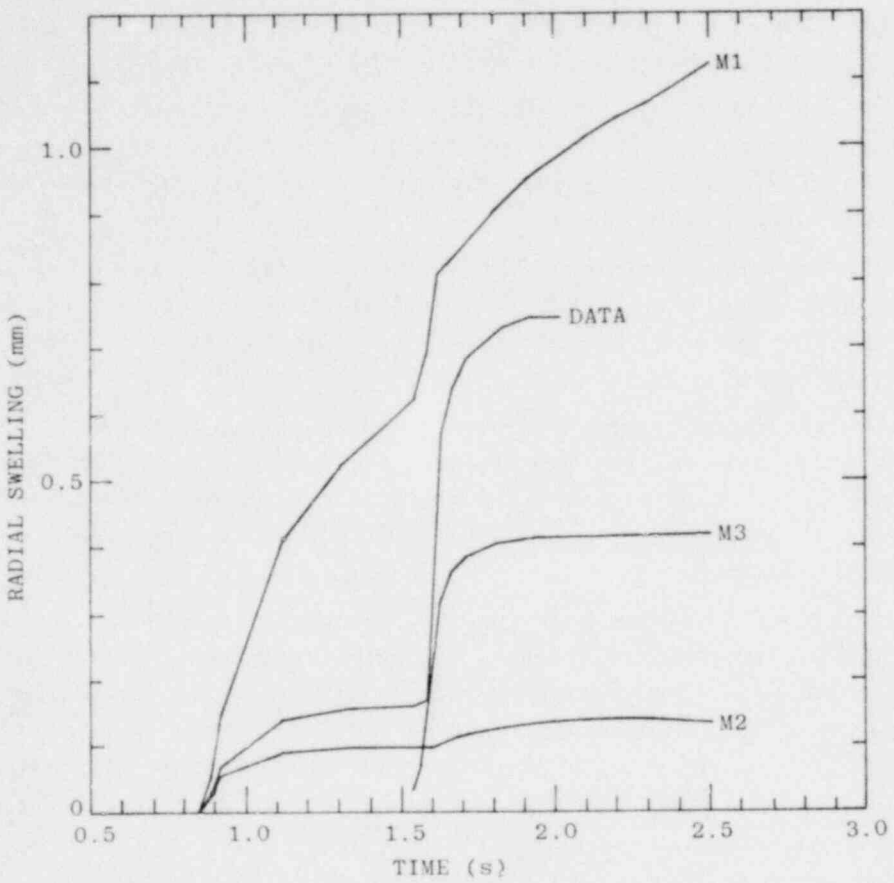

Figure 26. Comparison of FD 1.8 Data to Calculations.

1361 172

The comparison between the data and M2 (FRAS2 type) predictions is disappointing. One surprising result is the overprediction of swelling prior to the third pulse. This result is quite clear in Figure 26 for test 1.8. The onset of significant swelling is predicted to occur at the time of the second pulse; actual swelling starts at the third pulse. The same comments cannot be made for tests 1.4 and 1.7 because the cladding bulged away from the fuel and hid the actual fuel swelling. One could assume that the data extrapolates to very low swelling levels prior to the third pulse, but that would be speculative.

After the third pulse, the M2 model (FRAS2 equivalent) seriously underpredicts the observed swelling. If the physical constants were adjusted to obtain good agreement after the third pulse, the overprediction prior to the third pulse would become far more serious.

Note that large parameter variations are possible; there are large uncertainties in properties such as the bubble diffusion coefficient. The property values used here are those recommended by Gruber on the basis of an extensive parameter fitting study.[33]

A more serious problem with the M2 model is the failure to show a large response to the third pulse. This is most clear in Figure 25, where a large jump in measured swelling is contrasted to a prediction in which there is hardly a ripple after the third pulse. The M2 modeling is clearly inadequate to reproduce the data.

The M3 model results show the importance of fuel creep. Creep sharply reduces the excess swelling prior to the third pulse which occurs for M1 calculations. However, it is insufficient to reduce it to the extent that agreement with data is obtained. The most interesting effect of creep is to allow sudden swelling at the time of third pulse. This swelling occurs because of the very large sensitivity of creep rates to temperatures, an encouraging result suggesting that creep may be the source of the sudden swelling.

The swelling calculations for M2T (FRAS2 plus vacancy depletion; NEBRAS) are not plotted; the predictions fall along the abcissa. Vacancy depletion reduced intragranular bubble growth to the point where no macroscopic swelling can occur. This is a very significant result.

The vacancy depletion effect is a real one; M2T is the theoretical best-estimate model. The very serious discrepancy between theory and prediction leads to the idea that intragranular gas bubbles are not the source of the observed swelling but that gas on the grain boundaries must be considered.

3.6.4 Comparison of Data to Grain Boundary Swelling Models

In Figures 27, 28 and 29, the swelling data are compared to FISGAS calculations which include grain-boundary gas (M6, M8, M8A). The results presented in the graphs are based on an earlier version of FISGAS rather than on the final one. Although differences of swelling predictions of as much as 25% were noted, there are no significant qualitative differences. All of these calculations include the effect of nonequilibrium of intragranular bubbles, but this set of calculations does not include vacancy depletion.

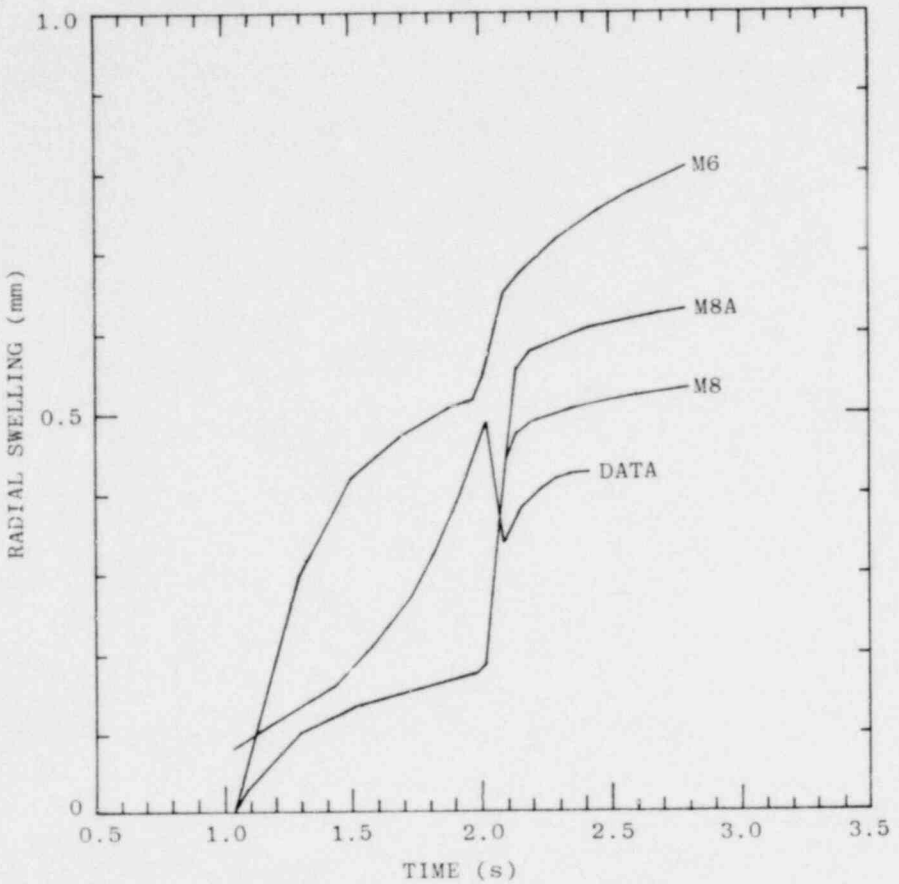

Figure 27. Comparison of FD 1.4 Data to Calculations.

1361 174

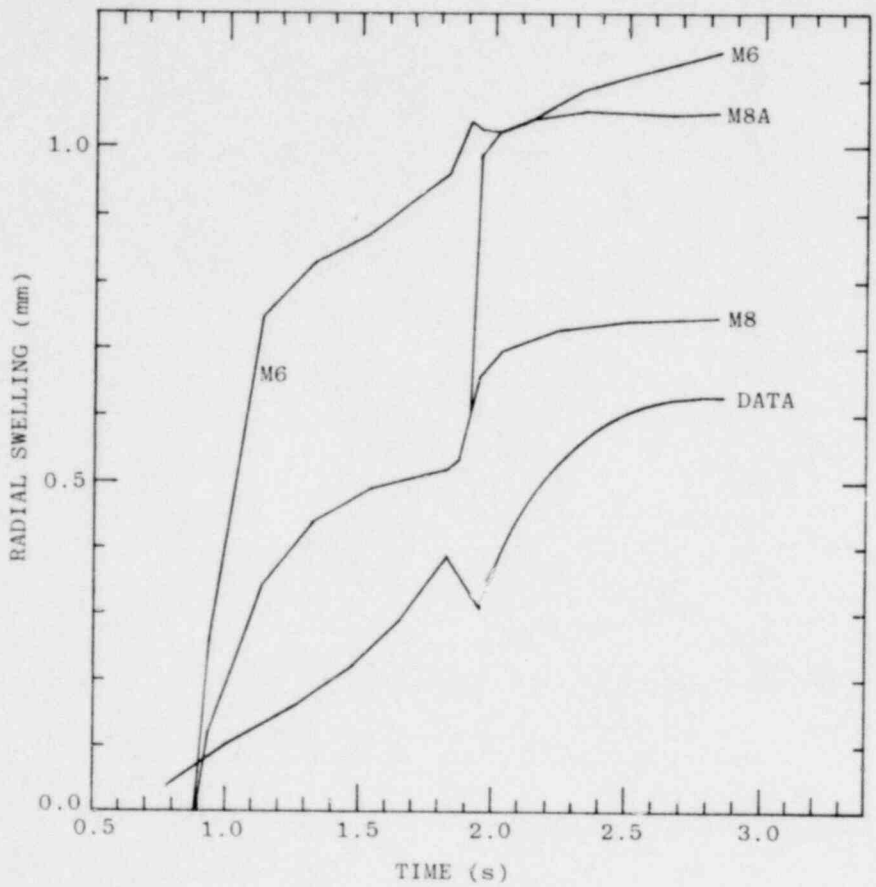

Figure 28. Comparison of FD 1.7 Data to Calculations.

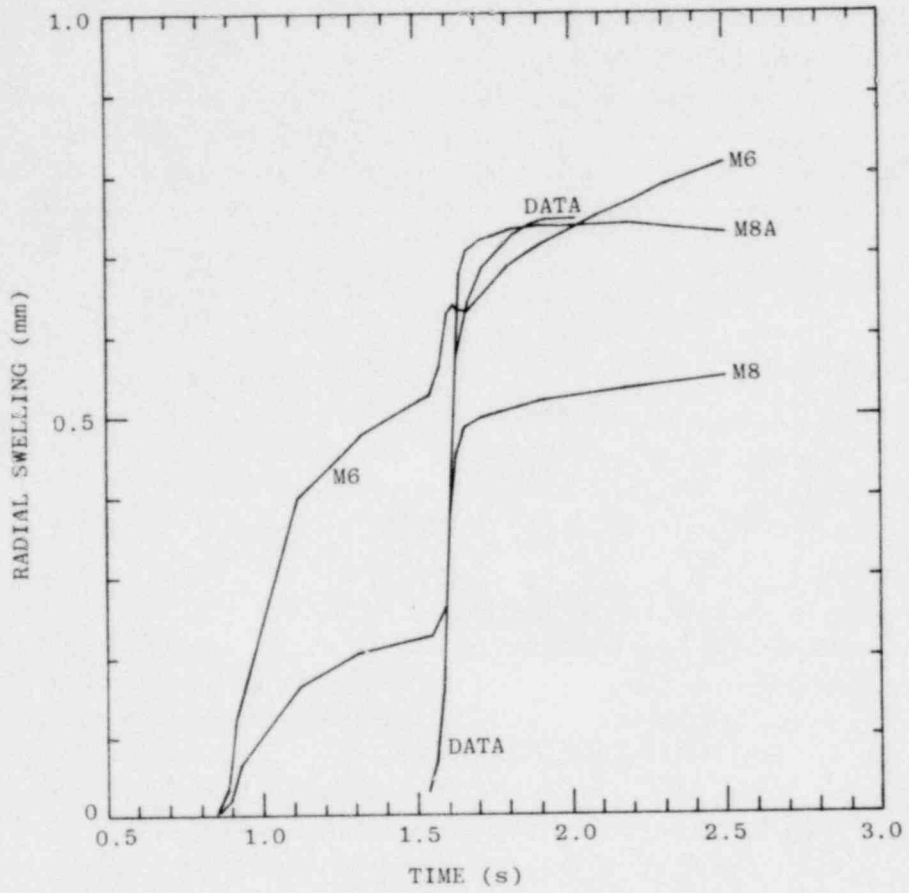

Figure 29. Comparison of FD 1.8 Data to Calculations.

The effect of creep restraint is most evident at lower temperatures, between the second and third pulse. The M8 calculations include fuel creep while the M6 calculations do not. The M6 calculations seriously overestimate early fuel swelling. Even with the creep restraint, there is a significant overprediction of early swelling. Creep also produces a much larger jump in swelling at the time of the third pulse, which brings the calculations into much better agreement with the data. Based on these calculations, fuel creep appears to be a necessary factor in explaining the FD test results.

The effect of grain edge gas on fuel swelling is relatively small. After the grain edge became saturated with gas, the grain boundary swelling is dominated by gas on the grain edge. Typically, the grain face swelling is an order of magnitude less than grain edge swelling. Thus, grain edge gas needs to be included in a complete model.

Most of the early excess swelling is caused by intragranular gas, although a substantial fraction, between the second and third pulses, is due to grain edge gas. Some modeling corrections appear to be needed.

Another modification to the basic FISGAS modeling was to allow relief from creep restrictions for any fuel node which exceeded the solidus temperature. These calculations, designated M8A, produce 50 to 100% greater jumps in swelling at the time of the third pulse. Some of the rapid swelling seen in the tests may be due to this effect.

In Figures 30, 31 and 32, the effect of vacancy depletion is explored. The swelling calculations are remarkably insensitive to vacancy depletion. The loss of early intragranular swelling in the M8T calculations is counterbalanced by an increase in early grain edge swelling. The increase in grain-boundary gas is due to the higher mobility of intragranular gas when those bubbles are kept small by vacancy starvation. Thus, the expected decrease in early swelling, due to vacancy depletion, does not occur. In this case, grain edge gas is clearly the source of the excess early swelling; modeling corrections for grain edge gas appear to be necessary.

The M8T calculations clearly demonstrate the need for grain edge gas in swelling predictions. Without grain edge gas there is little response from the fuel to the third pulse, which is in direct contradiction to the data. The sharp jump in swelling at the third pulse is apparently due almost entirely to grain edge gas.

3.6.5 Conclusions on Swelling Analysis and Calculations

The conclusions that may be drawn from the comparison of these calculations to the FD 1.4, 1.7 and 1.8 test data are as follows:

1. Grain boundary gas is required to explain the observed swelling;
2. Vacancy depletion is needed to eliminate excess predicted early intragranular swelling;
3. Too much early grain edge swelling is predicted, and model modifications are needed here;
4. The sharp jump in swelling at the third pulse probably is due to grain edge gas, which needs to be modeled separately from grain face gas;

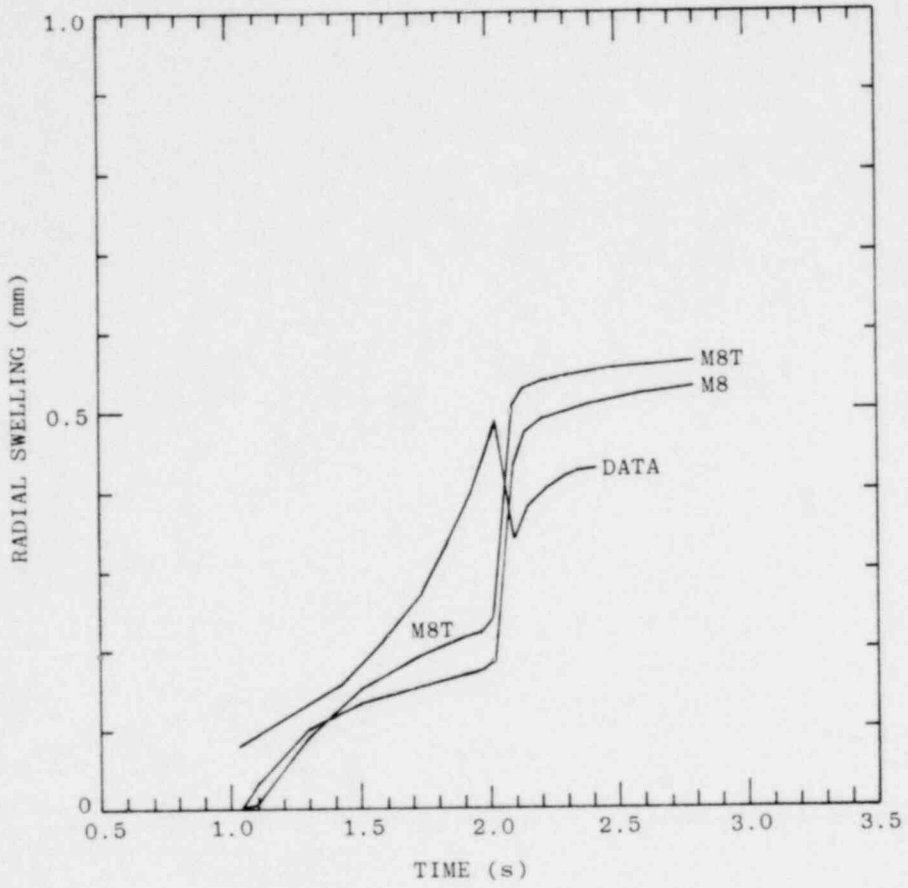

Figure 30. Comparison of FD 1.4 Data to Calculations.

1361 178

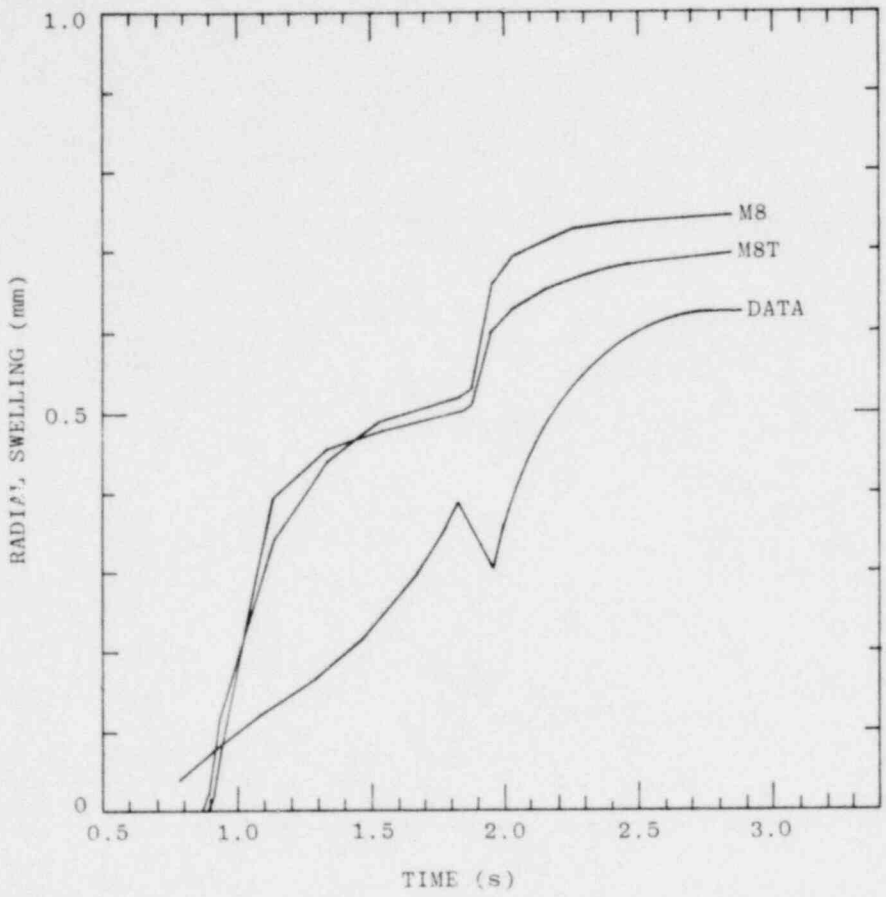

Figure 31. Comparison of FD 1.7 Data to Calculations.

1361 179

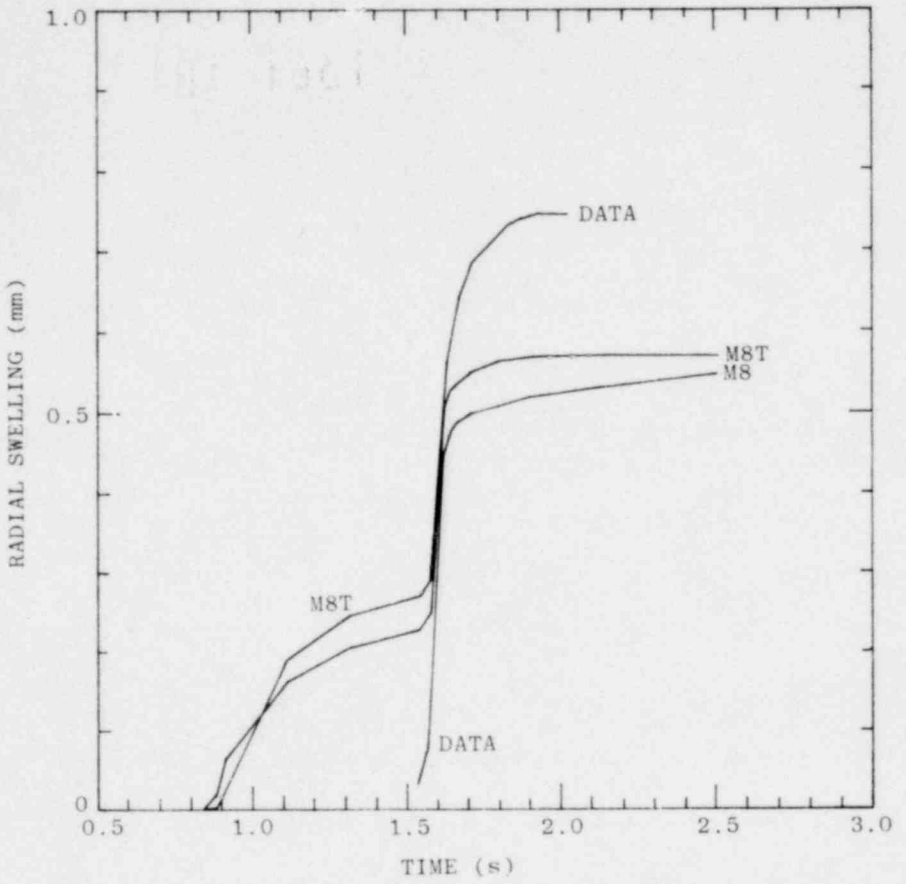

Figure 32. Comparison of FD 1.8 Data to Calculations.

1361 180

5. Some of the jump in swelling at third pulse may be due to fuel exceeding the solidus temperature and being relieved from creep restraint.

Further conclusions may be obtained from other swelling considerations, postmortem examination of the test fuel, and from data in subsequent test series.

4. Observations and Conclusions

The major observations and conclusions are that:

1. Rapid fuel swelling occurred, in the order of 0.1 second.
2. Extensive fuel swelling occurred, up to 67 areal percent, and may be the dominant early fuel disruption mechanism even under high power LOF conditions.
3. No evidence for dustcloud breakup or froth formation of fuel was seen for LOF timescales.
4. Fuel swelling observed is not predicted correctly by current, FRAS-type fission gas modelling.
5. FISGAS was developed as a result of 4.
6. Clad ballooned away from the fuel as the fuel swelled.
7. Stainless steel clad peeled cleanly off the fuel and on melting did not wet fresh UO_2 or PuO_2 fuel burned to 5 atom percent and at temperatures up to 3000 K.
8. The cinematographic diagnostic technique for recording in-pile fuel response was eminently successful.

5. Future Considerations and Investigation

The fuels used in three of the tests, FD 1.4, 1.7 and 1.8, swelled to varying degrees, depending on the power pulse, but did not otherwise disrupt. They provided basic swelling data, of a type not previously available. In addition, the fuel, together with a sibling fuel pellet and the fresh fuel used in FD 1.9, has been examined by means of light optical microscopy. The photography of the fuel under magnification to 500x has just been completed. The posttest analysis of the fuel will yield basic information on microscopic and macroscopic fuel response to the different transients for preirradiated and fresh fuel. Features such as generation and propagation of cracks, voids, melt fronts, limited bubble morphology and swelling characteristics and regions will be studied. Publication of the results will follow.

A comprehensive report on FISGAS, the Sandia transient fuel swelling and gas release code, now is complete. However, modifications in the model are continuing. A new calculation appears promising; it is based on intragranular bubble relaxation in the fuel as it achieves a plastic state or melt following a period of bubble coalescence and growth while the fuel, in the solid state is heating up. Here, intergranular gas does not play any role in fuel swelling nor does it provide a boundary saturation threshhold for gas release. This option may be included later in a new version of FISGAS.

Finally, a new series of fuel disruption experiments, FD-2, has been initiated. Significant improvements over FD-1 have been achieved in the geometry, diagnostics and fuel energetics. The most significant new features occur in the improved neutron intensity and energy spectra and power histories from the new Sandia Annular Core Research Reactor, ACRR. The undesirable neutronic and thermal end-effects on the FD-1 fuel have been effectively eliminated for this new series of tests. Thus prototypic[7,10] fuel heating rates and temperature profiles will be chieved. The geometry changes include fuel segments five times longer than in FD-1, and improved boundary conditions which assure flat axial temperature profiles. The improved diagnostics include, in addition to those used in FD-1, high-speed cinematography of both front and back of the fuel simultaneously during the power transient, real-time thermometry of the stainless steel clad, and sampling of gases which effuse from the fuel segment in the power pulse. These gases then will be analyzed spectrometrically posttest. Approximately ten tests will comprise the new series.

6. Acknowledgements

The authors acknowledge the many contributions and professional assistance by D. L. Fastle, R. M. Elrick, K. Reil, D. Sasmor, D. Pipher, F. Gonzalez, R.L. Coats, W.J. Camp, Personnel of CMB-14 and J.H. Scott of LASL, and the Sandia Reactor Operations personnel.

REFERENCES

1. F. E. Dunn, The SAS-3A LMFBR Accident Analysis Computer Code, ANL/RAS 75-17, Argonne National Laboratory, Argonne, Illinois (April 1975).

2. W. R. Bohl, J.E. Callahan, D.R. Ferguson, An Analysis of the Unprotected Loss-of-Flow Accident in the Clinch River Breeder Reactor with an End-of-Equilibrium Cycle Core, ANL/RAS77-15, Argonne National Laboratory, Argonne, Illinois (May, 1977).

3. J. L. McElroy, et. al., Clinch River Breeder Reactor Plant: An Analysis of Hypothetical Core Disruptive Events in the CRBR, CRBRP-GEFR-00103, UC-79P, General Electric Company, Sunnyvale, California (April 1978).

4. J. F. Meyer, et. al., An Analysis of the Clinch River Breeder Reactor Core Disruptive Accident Energetics, NUREG-0122, NRR, USNRC, Washington, D.C. (March 1977).

5. L. W. Dietrich and R. W. Ostensen, An Assessment of Fission-Gas-Driven Fuel Disruption and Dispersal in a Hypothetical LMFBR Loss-of-Flow Accident, ANL/RAS77-4, Argonne National Laboratory, Argonne, Illinois (February 1977).

6. L. W. Dietrich and J.F. Jackson, "The role of Fission Products in Whole Core Accidents-Research in the USA," IAEA Working Group on Fast Reactors, AERE, Harwell, UK (June-July 1977).

7. W.R. Bohl, et. al., An Analysis of Transient Undercooling and Transient Overpower Accidents Without Scram in the Clinch River Breeder Reactor, ANL/RAS 75-29, Argonne National Laboratory, Argonne, Ill. (July 1975).

8. C.A. Hinman and O.D. Slagle, Ex-reactor Transient Fission Gas Release Studies: Fuel Pin PNL 2-4, HEDL-TME-77-83 (May 1978).

9. M.H. McTaggart, J.R. Findlay, Progress Report on VIPER Measurements of Fission Product Pressure Generation, AWRE 44/96/4, SRD R123, Albermaston, Berks, England (July 1978).

10. W. Bohl, ANL, Private communication.

11. Optical train developed with R.M. Elrick and D.L. Fastle; ACPR power history diagnostics provided by K. Reil, Sandia Laboratories.

12. F.W. Sears, Optics, 313, Addison-Wesley (1949).

13. K.D. Lathrop and F.W. Brinkley, TWOTRAN-II: An Interfaced Exportable Version of the TWOTRAN Code for Two-Dimensional Transport, LA-4848-MS, LASL, NM (1973).

14. E. Wilmot, Sandia Laboratories, Private Communication.

15. L.L. Bonzon, F.M. Morris, F.V. Thome, Annular Core Pulse Reactor (ACPR): Experimenter's Manual, SLA-73-1017, Sandia Laboratories, Albuquerque, NM (October 1974).

16. G.I. Bell and S. Glasstone, Nuclear Reactor Theory, Van Nostrand Reinhold (1970).

17. T.F. Peterson, TAC2D-A General Purpose Two Dimensional Heat Transfer Code-Users Manual, GA-8868, Gulf General Atomic, San Diego, CA (1969).

18. Properties for LMFBR Safety Analysis, ANL-CEN-RSD-76-1, Argonne National Laboratory, Argonne, Illinois (1976).

19. Aerospace Structural Metals Handbook, 2, AFML-TR-68-115, Mechanical Properties Data Center, Belfour Stulen, Inc. (1976).

20. Y.S. Touloukian, Ed., Thermophysical Properties of High Temperature Solid Materials, Vol. 1, Macmillan (1967).

21. R. Bird, W. Stewart, and E. Lightfoot, Transport Phenomena, J. Wiley & Sons (1960).

22. D. Olander, Fundamental Aspects of Nuclear Reactor Fuel Elements, TID-26711-P1, National Technical Information Center, Springfield, Va. (1976).

23. M.L. Callabresi and S.T. Heidelberg Jr., "SASL: A Finite Element Code for the Static Analysis of Axisymmetric and Plate Solids Subjected to Axisymmetric and Plane Loadings," SCL-DR-720061, Sandia Laboratories, Livermore, CA (December 1972).

24. G. Bandyopadhyay, "Response of Oxide Fuel to Simulated Thermal Transients," Nuclear Technology, 40, 62 (1978).

25. R.J. Dimelfi and L.W. Deitrich, "The Effects of Grain Boundary Fission Gas on Transient Fuel Behavior," Nuclear Technology, 43, 328 (1979).

26. R.W. Ostensen, FISGAS--A Code for Fission Gas Migration and Fuel Swelling in an LMFBR Accident, SAND78-1790, Sandia Laboratories, Albuquerque, NM (July 1979).

27. E. E. Gruber, "A Generalized Parametric Model for Transient Gas Release and Swelling in Oxide Fuels," Nuclear Technology, 35, 617 (October 1977).

28. J.M. Griesmeyer, "Simulation of Intragranular Fission-Gas Behavior in Oxide Fuels," Ph.D. Thesis, UCLA (1978).

29. J.H. Scott, S.A. Chastain, T.T. Arey and E.D. Jenson, Preliminary Data Report; Post Irradiation Examination of Fuel Pins PNL 10-23 and PNL 10-63, HEDL-TME 74-23 Hanford Engineering Development Laboratory, Richland, WA (May 1974).

30. K.M. Case and P.F. Zweifel, Linear Transport Theory, p. 56, Addison-Wesley (1967).

31. J.H. Scott (Los Alamos Scientific Laboratory) private communication (1979).

32. D.S. Dutt, et. al., "A Correlated Fission-Gas Release Model for Fast Reactor Fuels," Trans Am Nucl Soc, 15, 198 (1972).

33. E.E. Gruber, Calculation of Transient Fission-Gas Release from Oxide Fuels, ANL 8143, Argonne National Laboratory, Argonne, Illinois (Nov 1974).

34. E.E. Gruber (Argonne National Laboratory) private communication (1978).

35. R.E. Esteves, A.R. Wazzan and D. Okrent, "Elementary Model for Non-Equilibrium Fission Gas Behavior in a Fast Transient," Trans Am Nucl Soc, 21, 180 (June 1975).

36. J.M. Griesmeyer, W.G. Steele, D. Okrent, S.H. Chien, and A.R. Wazzan, "A Non-Equilibrium Analysis of Fission-Gas Release and Swelling During Fast Transients", Trans Am Nucl Soc, 23, 174 (1976).

1361 186

DISTRIBUTION:

US Nuclear Regulatory Commission
(310 copies for R7)
Division of Document Control
Distribution Services Branch
7920 Norfolk Avenue
Bethesda, MD 20014

US Nuclear Regulatory Commission (54)
Division of Reactor Safety Research
Office of Nuclear Regulatory Research
Washington, DC 20555
Attn: C. N. Kelber, Assistant Director,
Advanced Reactor Safety Research
R. T. Curtis, Chief
Analytical Advanced Reactor
Safety Research, ARSR
M. Silberberg, Chief
Experimental Fast Reactor Safety
R. W. Wright (50)
Experimental Fast Reactor Safety

US Department of Energy
Office of Nuclear Safety Coordination
Washington, DC 20545
Attn: R. W. Barber

US Department of Energy (2)
Albuquerque Operations Office
P.O. Box 5400
Albuquerque, NM 87185
Attn: J. R. Roeder, Director
Operational Safety Division
D. K. Nowlin, Director
Special Programs Division
For: C. B. Quinn
D. Plymale

University of Michigan
Nuclear Engineering Department
Ann Arbor, MI 48104

General Electric Corporation
310 De Guigne Drive
Sunnyvale, CA 94086
Attn: J. O. Bradfute, Manager,
Dynamics and Safety

W. E. Nyer
P. O. Box 1845
Idaho Falls, ID 83401

Projekt Schneller Brueter (4)
Kernforschungszentrum Karlsruhe GMBH
Postfach 3640
D75 Karlsruhe
West Germany
Attn: Dr. Kessler (2)
Dr. Heusener (2)

Institut de Protection
et de Surete Nucleaire (3)
CEN Fontenay-aux-Roses
B. P. 6
92260 Fontenay-aux-Roses
France
Attn: M. Tanguy
M. Schmitt
M. Cogne

Safety Studies Laboratory (3)
Commissariat a L'Energie Atomique
Centre d'Etudes Nucleaires de Cadarache
B. P. 1, 13115 Saint-Paul-les-Durance
Bouches-Du-Rhone
France
Attn: M. Bailly
M. Meyer Heine
M. Penet

Centre d'Etudes Nucleaires de Grenoble
B. P. 85-Centre de Tri
38401 Grenoble, Cedex
France
Attn: M. Costa

H. J. Teague (3)
UKAEA
Safety and Reliability Directorate
Wigshaw Lane
Culcheth
Warrington, WA3 4NE
England

R. G. Bellamy
Reactor Fuels Group
AERE Harwell
Oxfordshire, OX11 ORA
England

R. G. Tyror, Head
Reactor Development Division
UKAEA - Atomic Energy Establishment
Winfrith, Dorchester
Dorset
England

Power Reactor & Nuclear Fuel
Development Corporation (PNC) (2)
Fast Breeder Reactor Development
Project (FBR)
9-13, 1-Chome, Akasaka
Minato-Ku, Tokyo
Japan
Attn: Dr. Mochizuki
Dr. Watanabe

1100 C. D. Broyles
Attn: G. E. Hansche, 1120
G. L. Ogle, 1125
H. E. Viney, 1130
J. H. Davis, 1136

1537 N. R. Keltner
R. U. Acton
T. Y. Chu
1550 F. W. Neilson
Attn: O. J. Burchett, 1552
J. H. Gieske, 1552

2150 T. L. Workman
3434 B. N. Yates
4000 A. Narath
4231 J. H. Renken
J. A. Halbleib
P. J. McDaniel
J. E. Morel

4400 A. W. Snyder
4410 D. J. McCloskey

1361 187

DISTRIBUTION: (Cont)

4420 J. V. Walker (5)
4422 R. L. Coats
4422 J. E. Gronager
4422 G. W. Mitchell
4422 J. B. Rivard
4422 D. W. Varela
4423 J. E. Powell
4423 G. L. Cano (10)
4423 A. C. Marshall
4423 J. G. Kelly
4423 D. A. McArthur
4423 H. L. Scott
4423 K. T. Stalker
4423 W. H. Sullivan
4423 S. A. Wright
4424 P. S. Pickard
4424 J. T. Hitchcock
4424 D. H. Worledge
4425 W. J. Camp
4425 R. W. Ostensen
4425 D. C. Williams
4425 M. F. Young
4425 R. J. Lipinski
4425 W. M. Breitung
4442 W. A. Von Riesemann
4450 J. A. Reuscher
4451 T. R. Schmidt
4452 L. D. Posey
5500 O. E. Jones
5511 M. L. Corradini
D. O. Lee
5530 W. Herrmann
5534 D. A. Benson
J. E. Smaardyk
5800 R. S. Claassen
5820 R. E. Whan
5822 N. E. Brown
5830 M. J. Davis
5831 J. L. Ledman
5831 N. J. Magnani
5831 D. A. Powers
5846 R. A. Sallach
E. K. Beauchamp
8266 E. A. Aas
3141 T. L. Werner (5)
3151 W. L. Garner (3)
For: DOE/TIC (Unlimited Release)
3154-3 R. P. Campbell (25)
For: NRC Distribution to NTIS

1361 188

10

POOR ORIGINAL

Org.	Bldg.	Name	Rec'd by *	Org.	Bldg.	Name	Rec'd by *

* Recipient must initial on classified documents.